The Astronomical Journal, 149:11 (26pp), 2015 January doi:10.1088/0004-6256/149/1/11

SPECTRAL CALIBRATION IN THE MID-INFRARED: CHALLENGES AND SOLUTIONS

G. C. Sloan[1], T. L. Herter[2], V. Charmandaris[3,4,5], K. Sheth[6], M. Burgdorf[7], and J. R. Houck[2]
[1] Cornell University, Center for Radiophysics and Space Research, Ithaca, NY 14853-6801, USA; sloan@isc.astro.cornell.edu
[2] Cornell University, Astronomy Department, Ithaca, NY 14853-6801, USA
[3] Department of Physics and ITCP, University of Crete, GR-71003, Heraklion, Greece
[4] Institute for Astronomy, Astrophysics, Space Applications & Remote Sensing, National Observatory of Athens, GR-15236, Penteli, Greece
[5] Chercheur Associé, Observatoire de Paris, F-75014, Paris, France
[6] National Radio Astronomy Observatory, 520 Edgemont Road, Charlottesville, VA 22903, USA
[7] HE Space Operations, Flughafenallee 24, D-28199 Bremen, Germany
Received 2013 May 31; accepted 2014 August 22; published 2014 December 10

ABSTRACT

We present spectra obtained with the Infrared Spectrograph on the *Spitzer Space Telescope* of 33 K giants and 20 A dwarfs to assess their suitability as spectrophotometric standard stars. The K giants confirm previous findings that the strength of the SiO absorption band at 8 μm increases for both later optical spectral classes and redder $(B–V)_0$ colors, but with considerable scatter. For K giants, the synthetic spectra underpredict the strengths of the molecular bands from SiO and OH. For these reasons, the assumed true spectra for K giants should be based on the assumption that molecular band strengths in the infrared can be predicted accurately from neither optical spectral class or color nor synthetic spectra. The OH bands in K giants grow stronger with cooler stellar temperatures, and they are stronger than predicted by synthetic spectra. As a group, A dwarfs are better behaved and more predictable than the K giants, but they are more likely to show red excesses from debris disks. No suitable A dwarfs were located in parts of the sky continuously observable from *Spitzer*, and with previous means of estimating the true spectra of K giants ruled out, it was necessary to use models of A dwarfs to calibrate spectra of K giants from observed spectral ratios of the two groups and then use the calibrated K giants as standards for the full database of infrared spectra from *Spitzer*. We also describe a lingering artifact that affects the spectra of faint blue sources at 24 μm.

Key words: infrared: stars

1. INTRODUCTION

The Infrared Spectrograph (IRS; Houck et al. 2004) on the *Spitzer Space Telescope* (Werner et al. 2004) has produced a rich legacy of scientific results, due in large part to its unprecedented sensitivity. One of the few drawbacks of such a powerful telescope is that bright objects saturate the detectors, eliminating most well understood infrared standard stars from consideration as calibrators.

Spectral calibration generally proceeds with the following equation

$$S_T = \frac{S_o}{C_o} C_T, \quad (1)$$

where all of the quantities are functions of wavelength. S_o and S_T are the observed and true spectra of the science target, respectively, and C_o and C_T are defined similarly for the calibrator (or standard star). The quantity C_T is the assumed spectrum of the calibrator, referred to hereafter as its *truth* spectrum. For ground-based spectrometers, the calibration varies with atmospheric conditions, requiring spectra of the standard and science target to either be corrected for differences in atmospheric transmission or be obtained at similar airmasses and at roughly the same time.

For space-based missions there is no atmosphere and the calibration is more stable. The problem then becomes one of determining a general spectral correction applicable as long as the responsivity of the instrument does not change. Previous satellite missions have defined a relative spectral response function $RSRF = C_o/C_T$ which can be used to calibrate the spectra of science targets: $S_T = S_o/RSRF$.

Any errors in the assumed truth spectra of the standards will propagate as artifacts into the entire database of calibrated spectra. For calibration of an instrument on a space-based mission, the challenge is to choose proper standards and define good truth spectra. The improved sensitivity of each new mission has revealed that we have more to learn about the stars chosen as standards.

The calibration of the *Infrared Astronomical Satellite* (*IRAS*) is a good example of the challenges. The *IRAS* team quickly discovered that α Lyr (A0 V), the primary photometric standard at all wavelengths, had an infrared excess beyond $\sim$20 μm due to a circumstellar debris disk (Aumann et al. 1984). Another surprise followed, as Cohen et al. (1992b) showed that the original calibration of the Low-Resolution Spectrometer (LRS) on *IRAS* produced an emission artifact in all of the spectra, due to the standard assumption at the time that K giants had featureless continua in the infrared.

The problem of assuming correct truth spectra for standard stars remains fundamental to infrared spectroscopy, despite the two decades that have passed between the *IRAS* and *Spitzer* missions. For the IRS, this issue was particularly acute. To avoid the danger of saturation, a standard star for the low-resolution IRS modules needed to be fainter than $\sim$2 Jy at 12 μm, which ruled out all of the previously calibrated standard stars. Thus, we had to start over with new standards.

The spectra calibrated by the *Spitzer* Science Center (SSC) met all pre-launch calibration requirements. This paper describes the efforts by IRS team members at Cornell and the SSC to improve on that effort. It concentrates on the observational findings made as part of that effort, both to justify some of the decisions made and to guide the calibration

of future infrared space telescopes. The sections below describe how we chose the standards for the IRS, determined their truth spectra, and analyzed the larger sample of candidate standards. The approach was iterative, with multiple definitions of truth spectra, tests, and improvements, making a linear presentation challenging.

In Section 2, we review methods used to estimate truth spectra of infrared standards before *Spitzer* launched. In Section 3, we describe how we chose candidate standards and how the calibration plan evolved during the *Spitzer* mission. Section 4 describes the observations, the Cornell data pipeline, and the construction of truth spectra and spectral corrections to calibrate all low-resolution IRS spectra. Section 5 examines actual coadded spectra for the standard stars observed most frequently and compares them to various truth spectra. A key finding is that our method does not propagate any identifiable artifacts into the IRS database. We also point out some of the shortcomings with traditional methods of estimating truth spectra. Section 6 focuses on the K giants, especially the SiO and OH absorption bands, which must be properly accounted for if they are to be used as standards. Section 7 concentrates on the photometric properties of the standards, both K giants and A dwarfs. Section 8 focuses on spectra of the A dwarfs, while Section 9 investigates the properties of the debris disks uncovered in our sample. Finally, Section 10 discusses our findings and draws some conclusions.

2. TRUTH SPECTRA

2.1. Composite Spectra

Prior to the work by Cohen et al. (1992b), K giants were commonly used as standards, with the assumption that their spectra could be modeled with a 10^4 K Planck function. The high temperature of the assumed Planck function mimics the effect of the H^- ion, which has an opacity that increases smoothly with wavelength, pushing the photosphere to cooler layers of the star at longer wavelengths. Engelke (1992) showed that a better fit to the continuum could be obtained with the Engelke function, which makes the brightness temperature of the star a smooth function of wavelength.

Cohen et al. (1992b) uncovered the presence of molecular absorption bands in the infrared spectra of late-type giants and documented their impact on the calibration of the *IRAS* spectra. To recalibrate the LRS database, Cohen et al. (1992a) started with A dwarfs, which can be modeled in a relatively straightforward manner. They based their calibration on α Lyr (A0 V) and α CMa (A1 V), relying on α CMa beyond 20 μm due to the red dust excess in the spectrum of α Lyr. Kurucz models (Kurucz 1979)[8] of these two stars served as the truth spectra for the calibration of other bright infrared standards.

Cohen et al. (1992b) produced a continuous and fully calibrated spectrum of α Tau (K5 III), primarily using α CMa as the calibrator and its Kurucz model as the truth spectrum. They built a composite spectrum of α Tau from spectral segments observed with a variety of ground- and space-based telescopes. They ensured photometric accuracy and continuity in the composite by pinning each spectral segment to infrared photometry. The resulting spectrum of α Tau showed multiple molecular absorption bands from the overtone and fundamental modes in CO and SiO. Cohen et al. (1992b) also published corrections for the LRS database by comparing their new spectrum of α Tau to the original LRS calibration.

Cohen et al. (1995) followed up with additional composite spectra of α Boo (K1.5 III) and four other giants, calibrated from Kurucz models of α Lyr and α CMa and the existing composite spectrum of α Tau. These composite spectra then served as the calibrators for further composite spectra (Cohen et al. 1996a, 1996b, 2003). Table 1 lists the 16 composite spectra produced using this method. These spectra have the advantage that the spectral features are as actually observed, based on spectral ratios with a fidelity that can be traced back to the original Kurucz models of α Lyr and α CMa.

Table 1
Primary Infrared Standards with Composite Spectra

Standard Star	Spectral Type	F_ν at 12 μm (Jy)[a]	Cohen et al. Reference	Used for Template	SWS Update[b]
α Lyr	A0 V	28.7	1992a	Y	⋯
α CMa	A1 V	98.7	1992a	Y	⋯
α^1 Cen	G2 V	153.2	1996a	⋯	Y
β Gem	K0 III	85.9	1995	Y	Y[c]
α Boo	K1.5 III	547.0	1995, 1996b	Y	Y
α TrA	K2 III	99.3	1996a	⋯	⋯
α Hya	K3 II-III	108.7	1995	Y	⋯
ϵ Car	K3 III	169.7	1996a	⋯	⋯
β UMi	K4 III	110.6	2003	⋯	Y
α Tau	K5 III	482.6	1992b	Y	Y
γ Dra	K5 III	107.0	1996b	⋯	Y
β And	M0 III	197.7	1995	⋯	Y
μ UMa	M0 III	69.6	1996b	⋯	Y
α Cet	M1.5 III	161.9	1996b	⋯	Y
β Peg	M2.5 II-III	267.1	1995	⋯	Y
γ Cru	M3.5 III	596.8	1996b	⋯	Y

Notes.
[a] Photometry from the *IRAS* Point-Source Catalog (PSC; Beichman et al. 1988) color corrected by dividing by 1.45.
[b] Short-Wavelength Spectrometer; Engelke et al. (2006).
[c] β Gem was not observed by the SWS; this spectrum was built from SWS observations of similar stars.

2.2. Spectral Templates

All of the sources in Table 1 are too bright for the mid-infrared calibration of the instruments on *Spitzer*. However, they can still serve as the basis for calibrating *Spitzer* through the process of spectral templating. Using the composite spectra of sources in Table 1 as prototypes, Cohen et al. (1999) created 422 spectral templates of fainter sources. Each templated spectrum is based on the composite spectrum of the bright standard with the same optical spectral class, after adjusting for differences in photometry and interstellar reddening. Sources with discrepant colors were excluded. The accuracy of the spectral template depends on the assumption that the infrared spectrum of a source can be accurately predicted from its optical spectral class. In preparation for the *Spitzer* mission, Cohen et al. (2003) expanded the wavelength coverage of their templates using optical spectroscopy for shorter wavelengths and Engelke functions for longer wavelengths. The resulting

[8] Kurucz (1979) describes the technique, but the individual models have been distributed outside the refereed literature. These models assume plane-parallel geometry and local thermodynamic equilibrium, as explained in more detail in his Section 4.2.

products, called supertemplates, were planned as the basis of the calibration of the Infrared Array Camera (IRAC) on *Spitzer*. They are generated using the same methods and assumptions as the earlier templates.

The spectral templates suffer from two limitations. First, because they are based on the actual observations that make up the composite spectra, they contain some noise. This noise is a minor issue for photometric calibration, but can be more significant for spectroscopic calibration. Second, some stars of a given spectral type may not have spectra identical to their prototype. Heras et al. (2002) found considerable variation in the strengths of the CO and SiO bands in the sample of late-type stars observed by the Short Wavelength Spectrometer (SWS) on the *Infrared Space Observatory* (*ISO*). Again, these variations affect spectroscopic calibration more than photometric calibration. The SWS sample contained a range of luminosity classes at most of the spectral classes examined, leaving open the possibility that variations in luminosity were responsible for the range of band strengths within each spectral class, but the size of the sample was too small to search for systematic trends.

2.3. Synthetic Spectra

The calibration of the SWS relied on many of the standard stars in Table 1 (Shipman et al. 2003; Schaeidt et al. 1996), but with synthetic spectra used for the truth spectra at shorter wavelengths. The synthetic spectra are free from noise, which is strong enough in the composite spectra to propagate through the calibration and into the SWS database.

However, Price et al. (2002) revealed that the synthetic spectra underestimated the strength of the SiO molecular band at 8 μm, and that the difference between observed and truth spectrum could propagate as an emission artifact into the entire SWS database. The difficulty with synthetic spectra of K giants lies in the atmospheric models on which they are based. The molecular absorption bands arise in rarified and extended layers of the atmosphere that have resisted accurate modeling (D. Carbon 2002, private communication). The errors in the modeled temperatures and densities as a function of radius lead to inaccurate profiles for the absorption bands (we return to this point in Section 6.4).

Synthetic spectra of earlier-type stars, such as A dwarfs, are more reliable. The observational problem is that A dwarfs are relatively rare compared to K giants among bright infrared targets, making it less likely they are located in readily accessible parts of the sky. For *Spitzer*, no A dwarfs suitable as standards could be found in the continuous viewing zones (CVZs).

3. THE CALIBRATION PLAN

3.1. Choice of Stellar Classes for Standards

When planning the spectral calibration of the IRS on *Spitzer*, we had to balance multiple challenges. K giants have two strong molecular absorption bands in the IRS wavelength range, the SiO fundamental at 8 μm and the CO fundamental at 5 μm. Using A dwarfs as calibrators would avoid these bands, but the hydrogen recombination lines in their spectra present their own problems. Any difference in the strength, position, or profile of these lines between the synthetic and observed spectra introduces narrow artifacts in the calibration. To match the line profiles in A dwarfs, one must convolve the synthetic spectrum with the correct unresolved line profile, which is a function of both wavelength and position in the slit. In addition, an offset of the position of the star in the dispersion direction (perpendicular to the long axis of the spectroscopic slit) will displace the lines in wavelength space.

Prior to the start of the *Spitzer* mission, we decided to use both the A dwarfs and K giants, using one group to mitigate for specific weaknesses in the other, since the K giants do not show atomic absorption lines in the infrared, and the A dwarfs do not show molecular absorption bands. We excluded M giants because of their deeper and more complex absorption bands and increased likelihood of variability. We did not consider solar analogues as potential standards because they are relatively uncommon and they are likely to show both molecular and atomic absorption features.

3.2. The Sample of Standard Stars

The sample of IRS standards was developed with multiple purposes in mind. Our primary goal was to observe a sufficient number to guarantee that after rejecting sources found to be inadequate for any reason, we still had enough sources to test the calibration for self-consistency. Second, we wanted to observe a statistically significant sample of stars of each spectral class, including A0 and A1 dwarfs and each subclass of K giant, in order to study how their spectral properties varied within each subclass and from one subclass to the next.

We selected several K giants in the CVZs, so that they could be observed in repeated IRS campaigns and help diagnose any variations in instrumental responsivity. With no suitable A dwarfs in the CVZs, we chose A dwarfs positioned around the ecliptic so that one or more would always be available. To provide sufficient temporal coverage and to sample spectral subclasses, we selected 20 A dwarfs. Because of uncertainties in the spectral classes, our A dwarfs included sources from B9 to A3. We did not observe later subclasses because they were not included in the original set of composite spectra. To properly sample the K giants, we observed ~5–6 of each subclass from K0 to K5, for a total of 33 K giants and 53 standards.[9]

Candidate standards had to meet a number of criteria. First, they had to have a reliable spectral type, with both a spectral class and a luminosity class and with little or no disagreement among published sources. For K giants, we required a luminosity class of "III," with no subtypes indicated, to see if we could reduce the scatter in band strengths observed by Heras et al. (2002). Photometry at *B*, *V*, and in the 12 μm *IRAS* filter had to agree with the colors expected for the star's spectral class. The [12]–[25] *IRAS* color had to be consistent with a naked star and not indicate a possible debris disk. For most of the standards observed during the scientific verification phase of the mission,[10] M. Cohen prepared spectral templates, using the methods described above. He fitted the templates to the available photometry, and some candidates were rejected at this stage.

Tables 2 and 3 present the K giants and A dwarfs ultimately observed by the IRS as potential standards and considered in this paper. The K giants are ordered by their dereddened

[9] This count does not include some fainter sources added later in the mission to test linearity or brighter sources used for the high-resolution modules.

[10] In 2003 November and December, between in-orbit checkout and the beginning of normal operations.

Table 2
The Sample of K Giants

Adopted Name	HR	HD	HIP	R.A. (J2000)	Decl. (J2000)	Spectral Type			F_ν at 12 μm (Jy)[c]	Observations	
						Literature	Reference[a]	Modified[b]		Total	Used
HD 41371	···	41371	28420	06 00 07.71	−64 18 36.0	K0 III	MC1	K0	0.372	1	1
HR 7042	7042	173398	91606	18 40 56.41	+62 44 58.1	K0 III	H55, E62	K0	0.800	2	2
HD 51211	···	51211	32813	06 50 25.27	−69 59 10.6	K0 III	MC1	K0	0.476	2	2
HR 6606	6606	161178	86219	17 37 08.88	+72 27 20.9	G9 III	H55	**K0**	1.143	64	36
HR 6348	6348	154391	83289	17 01 16.93	+60 38 55.5	K1 III	H55	**K0**	0.755	84	57
HR 2712	2712	55151	34270	07 06 14.31	−68 50 15.3	K0 III	MC1	K0	0.670	4	4
HR 1815	1815	35798	24256	05 12 25.76	−81 32 30.2	K1 III	MC1	K1	0.743	3	3
HD 59239	···	59239	35809	07 23 06.83	−70 38 11.8	K1 III	MC1	K1	0.574	5	5
HD 156061	···	156061	84494	17 16 27.69	−25 18 19.6	K1 III	MC4	K1	0.534[d]	2	2
HR 6790	6790	166207	88732	18 06 53.48	+50 49 22.2	K0 III	H55, E62	**K1**	0.797	4	3
HD 39567	···	39567	27436	05 48 35.14	−65 10 06.6	K2 III	MC1	**K1**	0.315	2	1
HR 7341	7341	181597	94890	19 18 37.87	+49 34 10.0	K1 III	H55	K1	0.996	74	29
HD 52418	···	52418	33306	06 55 40.95	−68 30 20.6	K2 III	MC1	K2	0.589	1	1
HD 130499	···	130499	72238	14 46 23.43	+56 36 59.0	K2 III	Y61	K2	0.672	2	2
HD 39577	···	39577	27564	05 50 16.54	−55 03 12.0	K2 III	MC1	K2	0.383	2	2
HD 115136	···	115136	64522	13 13 28.03	+67 17 16.7	K2 III	S60	K2	0.815	3	3
HD 50160	···	50160	32396	06 45 49.77	−70 31 21.6	K2 III	MC1	K2	0.361	4	4
HD 56241	···	56241	34381	07 07 42.68	−76 02 57.2	K3 III	MC1	K3	0.551	5	5
HD 42701	···	42701	28970	06 06 50.55	−67 17 00.0	K3 III	MC1	K3	1.121	2	2
HD 44104	···	44104	29820	06 16 48.05	−54 37 01.2	K3 III	MC1	K3	0.493	2	1
HD 23593	···	23593	17329	03 42 34.46	−64 11 43.1	K3 III	MC1	K3	0.738	2	2
HD 214873	···	214873	112021	22 41 25.65	−12 13 47.8	K2 III	MC4	**K3**	1.132	1	1
HD 19241	···	19241	14188	03 02 55.91	−60 47 51.9	K5 III	MC1	**K4**	0.859	3	3
HD 99754	···	99754	55981	11 28 23.34	−23 49 36.1	K4 III	MC4	K4	0.753	2	2
HD 166780	···	166780	88877	18 08 38.85	+57 58 46.9	K5 III	M50	**K4**	0.777	41	26
HD 214046	···	214046	111551	22 35 53.95	−20 56 05.2	K4 III	MC4	K4	0.689	2	2
HD 38214	···	38214	26751	05 41 01.53	−54 44 22.1	K5 III	MC1	**K4**	0.484	3	3
BD+62 1644	···	···	91691	18 41 52.39	+62 57 41.2	K3 III	C02	**K4**	0.272	3	3
HD 53561	···	53561	34258	07 06 05.03	+13 59 08.8	K5 III	M50	K5	0.855[d]	2	2
HD 15508	···	15508	11364	02 26 23.35	−68 38 07.2	K4 III	MC1	**K5**	0.576	2	2
HD 173511	···	173511	91673	18 41 40.59	+61 32 47.1	K5 III	M50	K5	0.814	132	84
HD 34517	···	34517	24559	05 16 10.06	−41 14 57.2	K5 III	MC2	K5	1.247	3	3
HD 39608	···	39608	27516	05 49 36.46	−60 40 34.7	K5 III	MC1	K5	1.001	1	1

Notes.
[a] The listed references are not meant to be complete. C02 = M. Cohen (2002, private communication), E62 = Eggen (1962), H55 = Halliday (1955), MC1, 2, 4 are the Michigan catalog, vol. 1, 2, and 4 (Houk & Cowley 1975; Houk 1978; Houk & Smith-Moore 1988), M50 = Moore & Paddock (1950), S60 = Stephenson (1960), and Y61 = Yoss (1961).
[b] Changes are in bold; see Section 6.3.
[c] Photometry from the *IRAS* Faint-Source Catalog (FSC; Moshir 1992) and color corrected by dividing by 1.45, unless noted otherwise.
[d] From the *IRAS* PSC and color corrected as the FSC data.

$(B–V)_0$ values as explained in Section 6.3. The A dwarfs are listed in order of right ascension.

3.3. Evolution of the Plan

When *Spitzer* was launched, two plans were in place for a parallel calibration of the spectra, one using synthetic spectra and one using spectral templates. As described above, each has strengths and weaknesses. Cornell focused on the spectral templates, while the SSC focused on the synthetic spectra. The Cornell team settled on three stars that behaved as expected, were relatively bright, and yet still faint enough to observe with the IRS Red Peak-up (PU) sub-array, which gave us photometry simultaneously with our spectra: HR 6348, HD 166780, and HD 173511. All were in or close enough to the northern CVZ to be observable from *Spitzer* most of the time.

HR 6348 became our primary standard because it had the weakest fundamental SiO band of the three. The SiO bandhead lies at 7.5 μm, right at the boundary of the two spectral orders in the Short-Low (SL) module, and choosing a standard with a weak band reduced any problems that might arise from inaccuracies in the band profile in our truth spectrum.[11]

[11] The 1σ pointing uncertainty of 0.″4 could produce a shift in the dispersion direction as large as 0.013 μm in SL1, which for HR 6348 would result in an apparent 0.1% artifact, due to an apparent shift between the actual bandhead and where it appeared in an observed spectrum. For HD 173511, which has a stronger SiO band, the effect would be 0.5% of the continuum, which is enough to be noticeable.

Table 3
The Sample of A Dwarfs

Adopted Name	HR	HD	HIP	R.A. (J2000)	Decl. (J2000)	Spectral Type		F_ν at 12 μm (Jy)[b]	Observations	
						Literature	Reference[a]		Total	Used
HR 1014	1014	20888	15353	03 17 59.07	−66 55 36.7	A3 V	E64, MC1	0.148	5	4
ν Tau	1251	25490	18907	04 03 09.38	+05 59 21.5	A1 V	S54, C69	0.783	2	2
η^1 Dor	2194	42525	28909	06 06 09.38	−66 02 22.6	A0 V	MC1	0.119	66	44
HD 46190	⋯	46190	30760	06 27 48.62	−62 08 59.7	A0 V	MC1	0.077	1	1
21 Lyn	2818	58142	36145	07 26 42.85	+49 12 41.5	A1 IV	S54	0.386	3	3
26 UMa	3799	82621	47006	09 34 49.43	+52 03 05.3	A2 V	M53, S54, E62	0.536	2	2
HR 4138	4138	91375	51438	10 30 20.13	−71 59 34.1	A1 V	MC1	0.418	9	7
τ Cen	4802	109787	61622	12 37 42.16	−48 32 28.7	A2 V	L72, MC2	0.937	7	5
ξ^1 Cen	4933	113314	63724	13 03 33.31	−49 31 38.2	A0 V	B60, MC2	0.335	3	3
HR 5467	5467	128998	71573	14 38 15.22	+54 01 24.0	A1 V	C69	0.115	49	38
HR 5949	5949	143187	78017	15 55 49.62	+58 54 42.4	A0 V	C69	0.080	4	4
δ UMi	6789	166205	85822	17 32 13.00	+86 35 11.3	A1 V	S54, E60	0.539	43	33
HD 163466	⋯	163466	87478	17 52 25.37	+60 23 47.0	A2	SIMBAD	0.090	48	34
HR 7018	7018	172728	91315	18 37 33.50	+62 31 35.7	A0 V	C69	0.134	27	18
λ Tel	7134	93148	175510	18 58 27.77	−52 56 19.1	B9 III	V57, B58	0.294	3	3
HD 165459	⋯	165459	88349	18 02 30.74	+58 37 38.2	A2	SIMBAD	0.076	2	2
29 Vul	7891	196724	101865	20 38 31.34	+21 12 04.3	A0 V	S54, E62, C69	0.311	17	9
ϵ Aqr	7950	198001	102618	20 47 40.55	−09 29 44.8	A1 V	E50, J53, M53	0.906	3	3
μ PsA	8431	210049	109285	22 08 23.01	−32 59 18.5	A1.5 IVn	G06	0.460	3	3
α Lac	8585	213558	111169	22 31 17.50	+50 16 57.0	A2 V	S54, E57	0.959[c]	28	19

Notes.
[a] The listed references are not meant to be complete. B58 = Buscombe & Morris (1958), B60 = Buscombe & Morris (1960), C69 = Cowley et al. (1969), E50 = Eggen (1950), E57 = Eggen (1957), E60 = Eggen (1960), E62 = Eggen (1962), E64 = Evans et al. (1964), G06 = Gray et al. (2006), J53 = Johnson & Morgan (1953), L72 = Levato (1972), M53 = Morgan et al. (1953), MC1 and MC2 are the Michigan catalog, vol. 1 and 2, (Houk & Cowley 1975; Houk 1978), S54 = Slettebak (1954), and V57 = de Veaucouleurs (1957). For the two entries labeled "SIMBAD," no further reference information about the spectral type could be found.
[b] Photometry from the *IRAS* FSC and color corrected by dividing by 1.45, unless noted otherwise.
[c] From the *IRAS* PSC; color-corrected like the FSC data.

It soon became apparent that the spectral template for HR 6348 (and the other standards) was insufficient as a truth spectrum. The apparent structure between 6 and 8 μm in the template for HR 6348 has a peak-to-peak amplitude of ∼3%, and this structure propagated from the template, which served as our initial truth spectrum to calibrate SL, to everything we calibrated with it. It was readily apparent in all IRS spectra with high signal-to-noise ratios (S/N). This structure originated in noise in the spectra used to construct the composite spectrum of β Gem, the prototype for the K0 spectral template.

We did not have synthetic spectra for HR 6348, HD 166780, or HD 173511, but the IRS spectra of standards that had been modeled, HR 6606 and HR 7341, confirmed our previous concerns about the ability of the synthetic spectra to accurately model the strength of the molecular absorption bands (see Section 5.3). Thus neither the templates nor the synthetic spectra would serve as truth spectra.

Fortunately, the large sample of potential IRS standards included two reasonably well-behaved and repeatedly observed A dwarfs, α Lac and δ UMi, putting us in a position to repeat the methodology of Cohen et al. (1992b). Where they calibrated α Tau from α Lyr and α CMa, we calibrated HR 6348 (K0 III) from α Lac and δ UMi. We then used the spectrum of HR 6348 to calibrate HD 173511, and with these two, all of the low-resolution spectra from the IRS on *Spitzer*. The following sections show that this approach produces self-consistent results for all of the standard stars observed.

We started with Kurucz models of a generic A2 dwarf, scaled to the photometry for α Lac and δ UMi. We estimate errors in the overall slope of the spectrum from differences between the assumed model and the actual stars by inferring blackbody temperatures from their B–V colors and the temperature calibration of Kenyon & Hartmann (1995). Across SL (i.e., 5–14 μm), these errors would be less than 0.5%, and across the full spectral range (5–37 μm), they would be 0.4% or less. As explained in Section 4.1, other systematic issues will dominate this error.

In order to calibrate HR 6348 with A dwarfs, we must mitigate for differences in the assumed and actual strengths and profiles of the hydrogen recombination lines in the A dwarfs, which will propagate to the spectrum of HR 6348. In our first attempt, we used polynomials to smooth the spectrum of HR 6348 in SL. In Long-Low (LL), we found that the shape of the spectrum was consistent with an Engelke function, but with structure due in part to noise and fringing. To remove these apparent artifacts, we replaced the LL spectrum with an Engelke function (Engelke 1992). Unfortunately, this step also removed real structure in the spectrum of HR 6348, primarily from OH bands in the 12–20 μm range (see Section 6.4). As a consequence, we finally decided to use the actual observed spectral ratios of HR 6348 to the A dwarfs at all wavelengths, mitigating for artifacts in the vicinity of recombination lines or from fringing only where these were clearly identifiable, as described in Section 4.3.

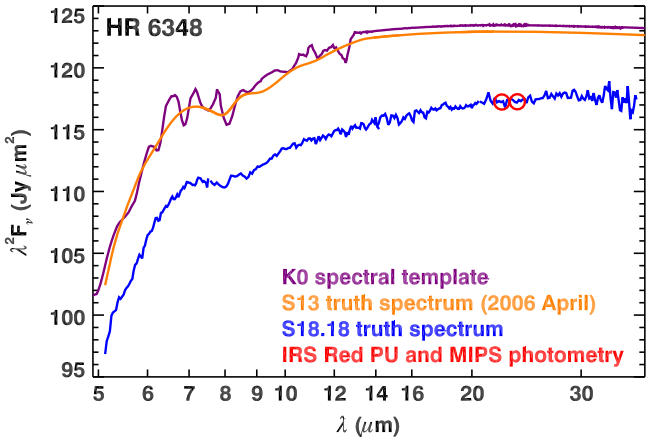

Figure 1. Evolution of the truth spectrum of HR 6348, our primary standard for the low-resolution modules. This and most other figures are plotted in Rayleigh–Jeans flux units, so that the Rayleigh–Jeans tail of a Planck function will be horizontal. The spectral template of a K0 giant (purple or darker upper trace) was the starting point. We shifted to a truth spectrum based on a heavily smoothed ratio between an A dwarf and HR 6348 (orange or lighter upper trace). The final truth spectrum for HR 6348 is shown on the lower trace, along with the photometry to which we forced it.

Concurrently with improvements in the quality of the truth spectra, we have also improved the photometric calibration of the spectra. Throughout, we have forced the spectra to be consistent with their Red PU photometry, but the PU calibration has changed. As described by Sloan & Ludovici (2011b), the Red PU calibration is now tied to the calibration of the 24 μm photometry from the Multi-band Imaging Photometer for *Spitzer* (MIPS) for HR 6348, HD 166780, and HD 173511 (Engelbracht et al. 2007), accounting for the difference in central wavelength (22.35 versus 23.675 μm). We originally forced the three spectra to the mean of the delivered spectral templates, shifting each to account for the relative PU photometry, then later to the mean *IRAS* FSC photometry (Moshir 1992) for these three sources. However, this mean was 5% too high compared to the 24 μm photometry, as shown in Figure 1. The 5% shift ties the current IRS calibration directly to the 24 μm MIPS calibration (Rieke et al. 2008).

4. DATA

4.1. Observations

The first set of usable observations of standard stars came in IRS Campaign P, which was executed 2003 November 14–16. Normal operations began on 2003 December 14, and every IRS campaign from then until cryogens were exhausted on 2009 May 15 included several observations of standards as part of what became known as the "calsfx" program.

This paper concentrates on the observations obtained with the two low-resolution IRS modules, SL and LL, which obtained spectra with resolutions ($\lambda/\Delta\lambda$) of roughly 80–120. Each module included separate apertures for first-order and second-order spectra. These are referred to, in order of increasing wavelength, as SL2, SL1, LL2, and LL1. When the star was placed in the SL2 or LL2 aperture, a small piece of the first-order spectrum was also obtained. These pieces are referred to as the bonus orders (SL-b or LL-b). Table 4 gives the usable wavelength ranges for each of the orders.

Table 4
Low-Resolution IRS Spectral Orders

Module and Order	Usable Wavelength Range (μm)
SL2	5.10–7.53
SL-bonus	7.73–8.39
SL1	7.53–14.20
LL2	13.95–20.54
LL-bonus	19.28–21.23
LL1	20.56–37.00

All spectra were observed in the standard staring mode of the IRS, which placed the target in two nod positions, one-third and two-thirds along each of the four low-resolution spectrographic slits. A typical low-resolution observation consisted of at least eight pointings, with two nods per aperture in both of the low-resolution modules.

Wherever possible, we peaked up on the standard itself, using the IRS Red PU sub-array (centered at 22.35 μm).[12] For faint targets, we used the Blue PU sub-array (16 μm). Targets brighter than ~1.0 Jy at 12 μm would saturate the PU sub-arrays, and for these, we generally peaked up with an offset star in the IRS PU sub-arrays. In all cases, we used the highest precision PU mode available, which generally placed the target within ~0.″4 of the nominal nod position. Self PU was the preferred mode because it required less accurate coordinates. As long as the target was the brightest source within ~ 45″ of the requested position,[13] the IRS would center it in the PU field and then shift it to the desired spectroscopic aperture.

Any pointing error in the dispersion direction (i.e., perpendicular to the long axis of the slit) would lead to truncation of part of the point-spread function (PSF) by the edges of the slit. This problem is known as spectral pointing-induced throughput error (SPITE), and it has been the subject of multiple IRS technical reports (e.g., Sloan et al. 2003; Sloan & Ludovici 2012a). The increasing size of the PSF with wavelength means that the slit throughput is a function of wavelength as well as position of the source within the slit. The general tendency is for more red flux than blue to be lost in the spectrum of a mispointed source, but the interaction of the slit edges and the Airy rings complicates this behavior.

SPITE is a significant issue for SL, because the typical pointing error (~0.″4) is a significant fraction of the distance from the center of the slit to its edge (1.″8). The problem was negligible in LL due to the larger slit width (10″).

To help reduce the impact of SPITE, we observed most of the standards described in this program at least two times. The only exceptions were the handful observed in Campaign P and not revisited during normal science operations. Some of the standards were observed much more frequently. HD 173511, for example, was observed in Campaign P and all 61 IRS campaigns during normal operations. Several other standards were observed frequently throughout the cryogenic mission (as can be seen in the last two columns of Tables 2 and 3).

[12] The peak-up operation uses the IRS imaging mode to determine the offsets necessary to properly center a target in the spectroscopic slits at the nod positions.
[13] This distance was reduced during the mission.

4.2. Data Reduction

We started with the S18.18 version of the SSC pipeline, with the basic calibrated data (BCD) files generated from the data cubes transferred from the spacecraft. These flatfielded images are the result of several steps in the SSC pipeline, most notably the removal of dark currents, mitigation for cosmic ray hits, and fitting of slopes to the signal ramps for each pixel. To generate a continuous spectrum from 5 to 37 μm, we follow a standard reduction algorithm that has now been applied to thousands of spectra published by the IRS Team at Cornell and the IRS Disks Team at Rochester.

First, suitable background images were subtracted from the on-source images. In SL, the default was to use the image with the source in the other aperture, referred to as an aperture difference. Thus, SL1 images served as the background for SL2 and vice versa. HD 46190 was the only exception, because the integration times in SL1 and SL2 differed. In LL, nod differences were the default, because the distance between the long slit length (150″) and the higher background levels relative to the emission from the stars left us more susceptible to residuals from background gradients.

Background-subtracted images were cleaned using the IMCLEAN software developed at Cornell[14] and the masks of rogue pixels generated for each campaign by the SSC. Rogue pixels are those with unstable responsivities or dark currents, preventing a proper calibration when subtracting the dark current from the data cubes or flatfielding the images. The SSC delivered one rogue mask per campaign, identifying all pixels identified as rogues during that campaign. We used those rogue pixel masks to generate cumulative rogue masks, which we updated every few campaigns. Any pixel identified as a rogue in at least two rogue masks from previous campaigns was marked as a rogue by us and cleaned. The number of rogue pixels generally increased during the mission due to the effects of space weathering. In addition to rogue pixels, we used the bit masks associated with each image to identify and clean pixels with invalid data, whether in the image with the source or the background.

To extract spectra from the images, we used the standard tapered-column extraction available with CUPID, the Customizable User Pipeline for IRS Data available from the SSC. This software is a copy of the offline pipeline. We used the PROFILE, RIDGE, and EXTRACT modules to identify the position of the source in the slit, map it onto the image, and extract it. For each wavelength element, a quadrilateral of roughly one pixel height was defined, tilted with respect to the row axis of the array to follow a line of constant wavelength. The width of the quadrilateral increases linearly with wavelength to follow the expanding size of the PSF. The downside of this algorithm is that it integrates noise from off-source pixels along with the source itself, but this is only a problem for faint targets, and our sample consisted primarily of bright stars.

We considered using the optimal extraction method developed at Cornell (Lebouteiller et al. 2010), which fits a PSF to the data at each wavelength to extract a spectrum. For sources as bright as ours, the gain in S/N is small, while the undersampled character of the PSF in SL2 and LL2 can produce small artifacts clearly visible at high S/Ns, degrading the quality of the spectra more than improving it. For fainter sources, the optimal extraction did improve the S/N of the resulting spectra, but for consistency, we used tapered-column extraction for all sources.

We extracted a spectrum from each image in a given nod position and then coadded them. We then calibrated the coadded spectra using the RSRF defined in the introduction. Spectra from the two nod positions were combined using a spike-rejection algorithm that identified and ignored any structure in one of the two spectra not present in the other. These steps gave us spectra in the four apertures: SL2 (plus SL-b), SL1, LL2 (plus LL-b), and LL1.

To determine uncertainties in the flux densities at each wavelength element, we measured the standard deviation σ when coadding all spectra in a given nod. The assigned uncertainty is the uncertainty in the mean ($\sigma/\sqrt{N}$). We re-evaluated the uncertainty when combining the nods, taking the larger of the propagated uncertainty and the uncertainty in the mean calculated from the data in the two nod positions.

To combine these spectral segments, we followed a "stitch-and-trim" algorithm. We applied scalar multiplicative corrections to each spectral segment to remove discontinuities between them, always normalizing upward to the (presumably) best-centered spectral segment. This usually meant that we scaled the two SL segments up to match LL. The bonus orders provided the overlap needed to scale SL2 to SL1 and LL2 to LL1. To scale SL1 to LL2, we used the small overlap of usable data (Table 4) between them. We then collapsed the bonus order data into the other orders by averaging where they overlapped and were within the range of valid wavelengths. All data outside the ranges given in Table 4 were trimmed from the spectra to produce the final spectra.

The last two columns in Tables 2 and 3 list the total number of spectra obtained in standard staring mode for each standard star as part of the spectral calibration program and the number we used when coadding spectra. The total number does not include spectra of some sources taken for other purposes, because these observations usually differed from the standard staring mode and were not suitable for spectroscopic calibration. The number used reflects spectra rejected for several possible reasons. The primary problem was reduced fluxes because of pointing errors, which could distort the shape of the spectra (Sloan & Ludovici 2012a). Other spectra were rejected because they showed evidence of residual images from previously observed bright sources, data drop-outs, or other artifacts that indicated some problem with the observation.

4.3. Constructing Truth Spectra

To generate the truth spectra, we started with HR 6348, α Lac, and δ UMi, generating ratios of observed spectra and calibrating them with scaled Kurucz models of the A dwarfs. Sloan & Ludovici (2012b) describe our method for SL, and Sloan & Ludovici (2012c) combine LL and the combination of SL and LL into a single low-resolution truth spectrum. We refer the reader to these reports for any questions not answered by the more brief description provided here.

4.3.1. Short-Low

The SL wavelength grid is finer than in LL, requiring more attention to possible artifacts arising from differences in assumed and observed profiles of the hydrogen recombination lines in the A dwarfs. For the spectra from each nod position, we calibrated HR 6348 separately with each of the two A

[14] This algorithm was included in the IRSCLEAN package distributed by the SSC.

dwarfs, then combined them using a spline to force them to their mean shape and strength while preserving detailed differences between them. When one spectrum showed more structure than the other, we dropped the affected wavelengths from that spectrum from consideration. We then combined the spectra from the two nods similarly, repeating the same sequence for SL1, SL2, and the SL-bonus order.

The resulting SL spectrum of HR 6348 shows some structure in the vicinity of the recombination lines, most notably in the immediate vicinity of 7.46 μm, where Pfund-α blends with three other recombination lines. We generated a correction to the spectrum of HR 6348 at Pfund-α based on how the artifact propagated to spectra of the asteroids Amalia and Isara and the ultraluminous infrared galaxy *IRAS* 07598+6508. These three sources should show a smooth red spectrum in this position, and with them, we were able to reduce the deviations at Pfund-α to $\sim$0.8% of the continuum (from $\sim$1.5%). What remains could be an artifact, or it could be intrinsic to the spectrum of HR 6348. We were unable to reduce the apparent structure in the vicinity of other recombination lines, which can reach $\sim$0.5% of the continuum. Thus, our truth spectra should propagate no apparent spectral structure into other IRS spectra up to a S/N of $\sim$120 at 7.5 μm and 200 elsewhere.

4.3.2. Long-Low

In LL, the spectra from the two nod positions showed no significant differences, so we first combined them with a simple average and then concentrated on the differences in ratios of HR 6348 with α Lac and δ UMi which arise from an apparent red excess in α Lac (Section 5.1 below). When calibrated with α Lac, the LL1 spectrum of HR 6348 is bluer than a Rayleigh–Jeans tail, which is unphysical, while the spectrum calibrated with δ UMi behaves more reasonably. The spectra in LL2 and the bonus order also showed similar differences depending on which A dwarf was used. These results confirm the red excess in α Lac. To mitigate, we used a spline function to force the shape of the two calibrations of HR 6348 to match that of the calibration with δ UMi while preserving the finer differences between the two. We applied the same procedure to each of the three spectral orders.

Many of the LL1 spectra in the IRS database are affected by fringing, and despite the many spectra coadded to produce the truth spectrum of HR 6348, this fringing did not cancel out. We corrected for the fringing by fitting a polynomial to the spectra of two red sources expected to show a smooth continuum at these wavelengths, *IRAS* 07598+6508 and Mrk 231, and assuming that the differences between the polynomial and the spectra arise from fringing. Because the fringing in the red sources is roughly twice as strong as in HR 6348, we reduced the correction by a factor of two before applying it. We also limited the correction to wavelengths below 32 μm because the data and the correction grow more unreliable to the red.

The dominant remaining structure in the LL spectrum of HR 6348 is real and arises from OH absorption, a point discussed more fully in Section 6.4 below. The OH band structure is strongest in LL2, where it produces an apparent corrugation similar to the fringing in LL1. For that reason, we avoided using Fourier analysis to defringe, since that would remove any periodic structure from the spectrum.

Early in the mission, we assumed that an Engelke function was a suitable model for the long-wavelength spectrum of HR 6348 (and other K giants). The omission of the OH contribution introduced an artifact in LL2 in early Cornell calibrations, which, while small, was noticeable in spectra with high S/Ns.

4.3.3. The Combined Low-resolution Truth Spectrum

Normally, the stitch-and-trim step is the final step, leaving us with a spectrum normalized to what is presumably the best-centered spectral segment. However, when generating truth spectra, we can force them to match the Red PU photometry by shifting them multiplicatively. As explained in Section 3.3, Sloan & Ludovici (2011b) have calibrated the Red PU photometry to align with the calibration of MIPS-24 (Rieke et al. 2008), so this last step cross-calibrates the IRS directly with MIPS.

The scalar multiplicative corrections made in the stitch-and-trim step and when shifting the spectrum to match the PU photometry do not correct for any distortions in the shape of the spectra from pointing-related errors (SPITE; Section 4.1). These distortions will ultimately limit the absolute calibration of the spectra. Sloan & Ludovici (2012c) estimate that the overall fidelity of the shape of the SL portion of the truth spectrum of HR 6348 is good to within 2%. This fidelity should not be confused with the point-to-point, or spectroscopic uncertainties, which are smaller, as noted in Section 4.3.1. Sloan & Ludovici (2012c) estimate that the fidelity in LL is better than 0.5% to the blue of $\sim$29 μm and $\sim$1% to the red, primarily due to limitations in the S/N.

Sloan & Ludovici (2012c) generated a truth spectrum for HD 173511, using HR 6348 as the calibrator, based on data up to IRS Campaign 44 (2007 October 7). The detector settings of LL changed with the beginning of IRS Campaign 45 (2007 October 29), requiring an independent calibration for LL spectra from that time to the end of the cryogenic mission. The fidelity of this spectrum is similar to that of HR 6348.

4.4. Spectral Corrections

To use a truth spectrum to calibrate data from the IRS, we created a spectral correction, or RSRF, as defined in Section 1. This correction is a full vector correction, meaning that each wavelength is treated independently, and it differs from the corrections used in the SSC pipeline. The SSC corrections are polynomials fitted to the full vector, are smoother, and do not account as well for wavelength-to-wavelength variations.

At the beginning of the *Spitzer* mission, we adopted separate spectral corrections for spectra obtained in the two nod positions in all low-resolution orders. We anticipated that as the quality of the flatfield corrections improved, these differences would work their way into the flatfield and we could eventually adopt a single spectral correction for all pointings in a given order. Nonetheless, at the end of the mission, the differences in the raw nod spectra are still significant enough to warrant independent corrections.

To generate spectral corrections, we used HR 6348 for all SL data and for all LL data up to Campaign 44. HR 6348 was not observed enough times after the changes to LL to generate a spectral correction with a sufficiently high S/N. Consequently, we use both HR 6348 and HD 173511 to calibrate LL data from Campaigns 45–61.

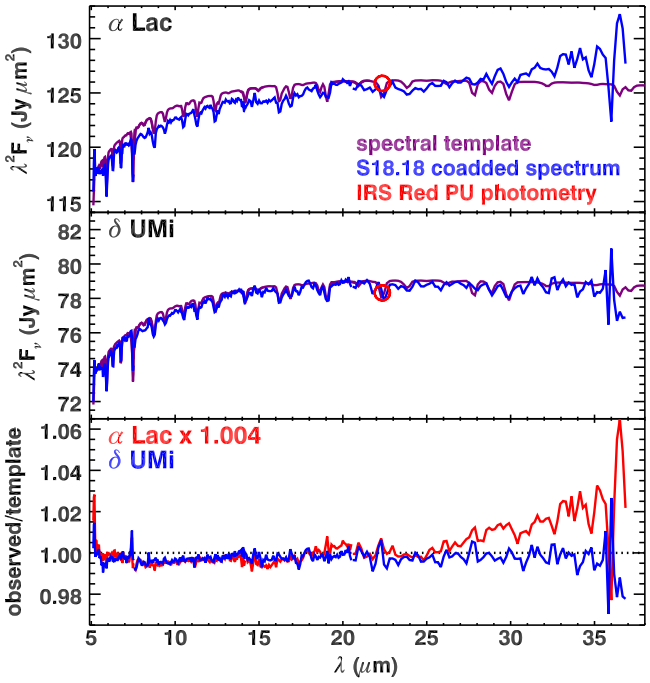

Figure 2. Templates and coadded low-resolution IRS spectra of the A dwarfs α Lac (top) and δ UMi (middle). The template is a scaled Kurucz model, and the differences between it and the coadded spectra reflect the fidelity of the shape of the IRS spectra for well-pointed sources. The red excess in α Lac beyond 25–30 μm is a different matter. The bottom panel compares the ratios of the two spectra to their templates. We have shifted the spectrum of α Lac up by 0.4% to demonstrate that the SL spectrum (below 14 μm) is unaffected by this excess, which we suspect arises from a low-contrast debris disk.

The spectral corrections currently available in SMART[15] are generated as described above. The spectral corrections are available for the tapered-column extraction in SMART, which is functionally equivalent to the method used by CUPID. They are also available for optimal extraction (Lebouteiller et al. 2010). Spectral corrections can be generated for any extraction method, as long as the standards are extracted identically to the science targets.

4.5. Spectral Atlas

The spectra of all of the stars listed in Tables 2 and 3 are also publicly available. They can be obtained from the Infrared Science Archive (IRSA), VizieR, or directly from the first author's website. Each spectral file has the following columns: wavelength (μm), flux density and uncertainty (Jy), and spectral order number (2 = SL2, 1 = SL1, 5 = LL2, 4 = LL1).

5. CHECKING THE CALIBRATION WITH OTHER STANDARDS

5.1. α Lac and δ UMi

Figure 2 compares the coaddition of all of the unrejected spectra of the A dwarfs α Lac and δ UMi to the Kurucz models with which the calibration started. At a minimum, we should get back what we started with, and for δ UMi, we do, to within better than ~0.5% at all wavelengths, except at Pfund-α, which differs by ~1% in total depth.

The observed coadded spectrum of α Lac differs from the Kurucz model in two ways. The difference in overall photometric level is attributable to the accumulated impact of small pointing errors, but, as described by Sloan & Ludovici (2012c), the observed spectrum shows a small red excess. If measured starting at 22 μm, it has a strength of ~2.5% by 35 μm. The cause is most likely a low-contrast debris disk around α Lac. Section 4.3.2 explains how we addressed this problem when calibrating LL.

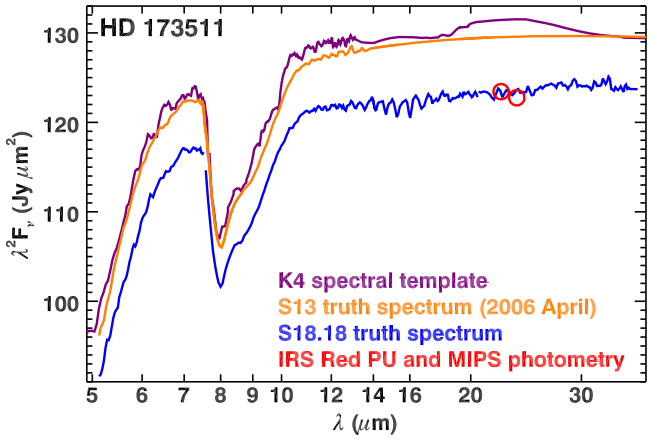

Figure 3. Comparison of the various truth spectra of HD 173511. The shift between early versions and the final truth spectrum reflects the shift in photometric calibration. The structure in the S18.18 truth spectrum between 10 and 20 μm is real and arises from OH. The spectral template was based on a K4 giant, but we now classify the star as K5 III.

5.2. HD 173511 and HD 166780

Early in the mission, HD 166780 and HD 173511, both late K giants, were used to supplement HR 6348 when calibrating LL, due to the lower S/N of blue sources in LL compared to SL and the limited number of HR 6348 observations available at the time. As described by Sloan & Ludovici (2011a), HD 166780 exhibited more variability in the Red PU data than the other standards considered, and as a consequence we dropped it as an IRS standard. The MIPS 24 μm photometry also hints at possible variability.

Figure 3 illustrates the evolution of the assumed truth spectra for HD 173511. Prior to launch we reclassified HD 173511 as a K4 III.[16] The K4 spectral template is based on an average of the prototypes for K3 and K5, α Hya and α Tau, and both stars are bright enough to produce a composite spectrum with an excellent S/N. The template matches the depth and shape of the observed SiO profile well. The primary deficiency in the template occurs at wavelengths past 13 μm, where the template shows a broad plateau at ~20 μm not apparent in the S18.18 truth spectrum. The older S13 truth spectrum in the figure used an Engelke function past 14 μm and is thus not a good test. It is possible that the apparent dip in the template from 13 to 20 μm could reflect in part the effect of OH band absorption in α Tau, but the downturn past 23 μm is not real.

[15] The Spectroscopy Modeling Analysis and Reduction Tool; see Higdon et al. (2004).

[16] Based on its $(B–V)_0$ color, we reclassified HD 173511 back to K5, as explained in Section 6.3.

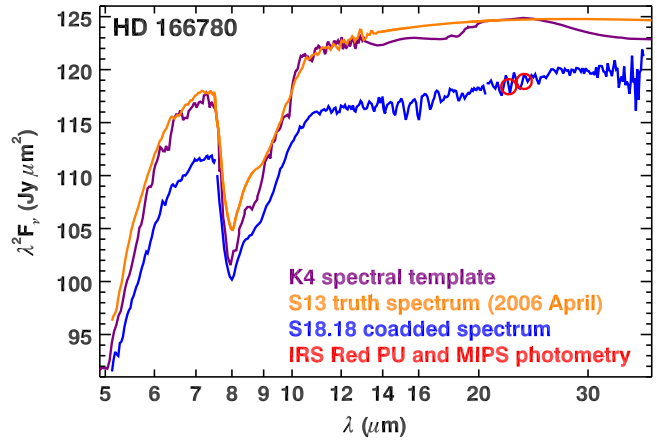

Figure 4. Evolution of the spectrum of HD 166780. For the S18.18 spectrum, we use a coadded spectrum from all of the unrejected observations because we did not generate a final truth spectrum. The agreement with the photometry is fortuitous.

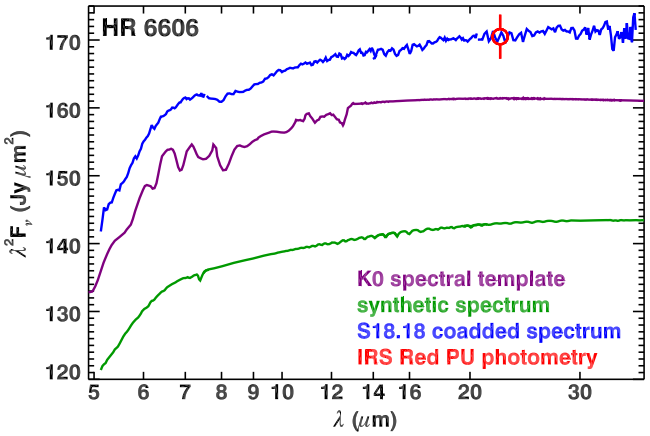

Figure 5. Candidate truth spectra for HR 6606. The synthetic spectrum is from Decin et al. (2004).

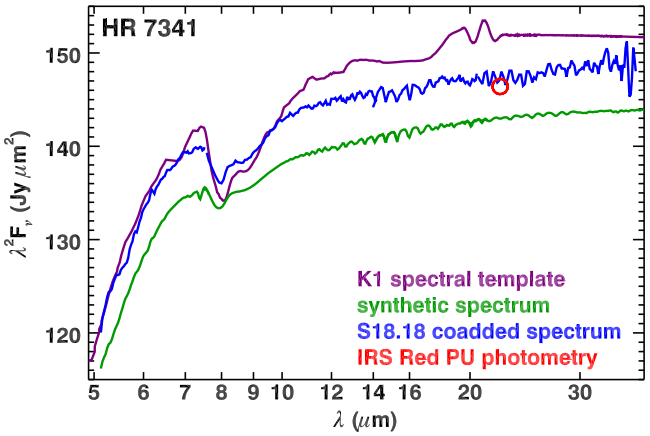

Figure 6. Candidate truth spectra for HR 7341. The synthetic spectrum is from Decin et al. (2004). The spectral template overpredicts the strength of the SiO band at 8 μm, while the synthetic spectrum underpredicts it; neither is suitable as a truth spectrum.

Figure 4 compares the spectra of HD 166780. We reclassified it as K4 prior to launch, like HD 173511, which means that their spectral templates only differ photometrically. Because HD 166780 is no longer an IRS standard, we do not plot an S18.18 truth spectrum; rather, we have presented the coaddition of unrejected spectra with no other adjustments. The issues past 13 μm are similar to HD 173511. More importantly, the SiO absorption band at 8 μm in HD 166780 is weaker than in the template, showing that the templates cannot be relied upon to match the profile of the absorption bands.

5.3. HR 6606 and HR 7341

Figures 5 and 6 illustrate the challenges of predicting the infrared spectral properties of K giants from their photometry. The spectral template of HR 6606 is based on β Gem (like HR 6348), while the template for HR 7341 is based on a weighted average of β Gem (K0) and α Boo (K1.5). The synthetic spectra are from Decin et al. (2004).[17] The S18.18 spectra are a coaddition of all good spectra observed by the IRS. The alignment with the PU photometry indicates the photometric quality of the coadded spectra.

We rejected HR 6606 early in the mission because it was unusually bright compared to expectations, and it was brighter than recommended for peaking up with the IRS Red PU array. We did manage to obtain one PU measurement, which is shown in Figure 5. The spectral template contains the same pattern noise seen in HR 6348.

The synthetic spectrum of HR 6606 predicts no measurable SiO absorption, but the observed IRS data clearly show this band. Similarly, in HR 7341, the synthetic spectrum underpredicts the strength of the band. Section 6.2 shows more quantitatively that the observed SiO bands are always deeper than expected from the synthetic spectra. We conclude that the synthetic spectra should not be used as truth spectra for spectroscopic standards.

The SSC adopted HR 7341 as their primary low-resolution IRS standard. Their use of its synthetic spectrum for a truth spectrum propagated an SiO artifact into the SSC calibration of the full database of SL spectra. While the size of the artifact is small, only ~1.5% at 8 μm, it was large enough to be noticed by Ardila et al. (2010), who published an atlas of stellar spectra observed by SL and LL. They found the artifact in all of their spectra and corrected it with a polynomial fitted to the ratio of the observed spectrum of α Lac to its spectral template (i.e., a Kurucz model). The spectral template for HR 7341 would not solve this problem, because it overpredicts the strength of the SiO band, making it equally unsuitable. The SiO artifact remains in all spectra in the S18.18 pipeline from the SSC.

The synthetic spectra of both HR 6606 and HR 7341 show a narrow absorption feature centered at 7.39 μm not identified by their creators. This is close to the Pfund-α complex at 7.46 μm, but shifted enough to the blue that it would have to be blended with another feature or be a different feature entirely. While our truth spectrum of HR 6348 does have weak Pfund-α absorption, it is likely an artifact from the use of A dwarfs to calibrate it. Our calibration of the K giants, which is based on the observed ratios of A dwarfs and HR 6348, does not reproduce this 7.39 μm feature.

We have described the shortcomings of the synthetic spectra and spectral templates, but the coadded spectra also have

[17] All of the synthetic spectra utilized in this paper are available at http://irsa.ipac.caltech.edu/data/SPITZER/docs/irs/calibrationfiles/decinmodels/. These spectra were synthesized using plane-parallel models for the G9 giants and spherically symmetric models for the later spectral classes (Decin et al. 2003b).

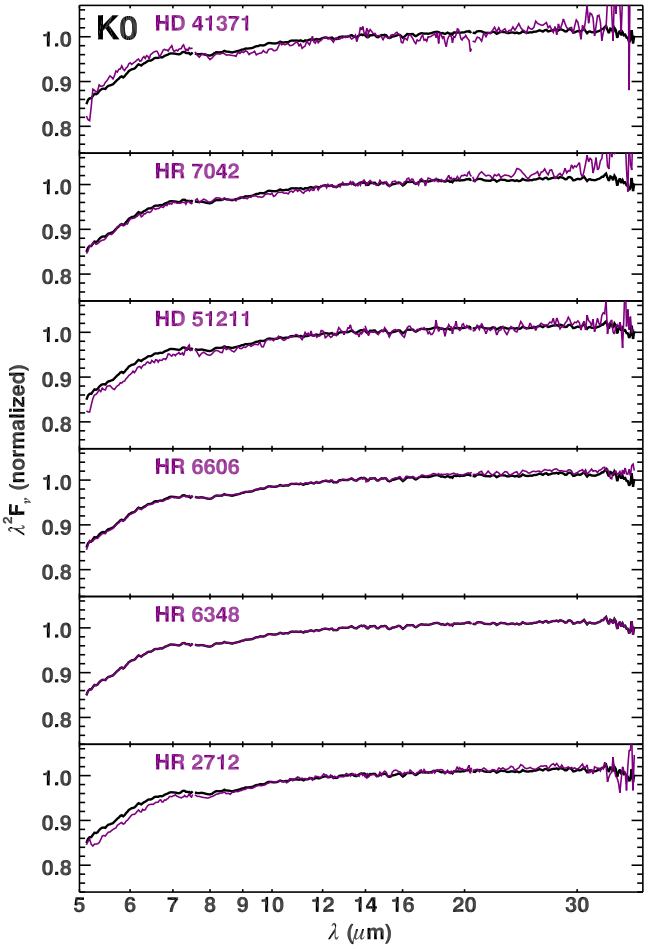

Figure 7. IRS spectra of the K0 giants in Rayleigh–Jeans units, and with the spectrum of HR 6348 overplotted as the prototype in each panel in black.

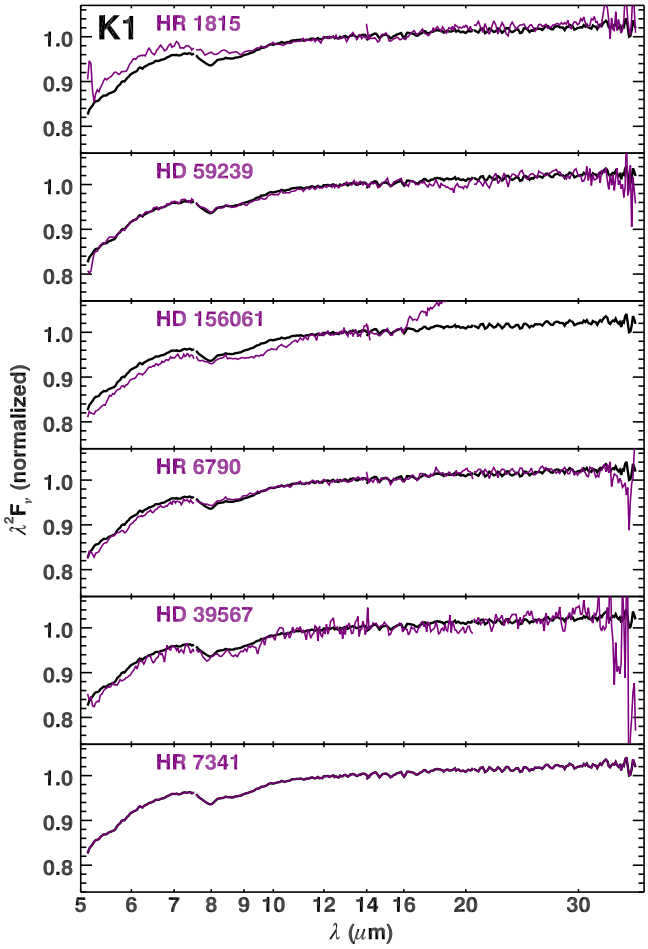

Figure 8. IRS spectra of the K1 giants, plotted as in Figure 7. HR 7341 is the prototype and is plotted in black in each panel. The spectrum of HD 156061 shows a strong red excess, which may arise from a debris disk (see Section 9.1).

problems. Past 20 μm, the spectra of both HR 6606 and HR 7341 show a periodic structure with a peak-to-peak amplitude of $\sim$1%. The synthetic spectra of both stars show that the structure due to OH should be much weaker at these wavelengths compared to the OH band structure at $\sim 14 - 16\,\mu$m. While it is possible that OH could be contributing to the observed structure past 20 μm, it is far more likely that it is due to fringing in LL1.

Thus, we have no perfect solutions to the problem of generating truth spectra for K giants. While truth spectra based on observed spectral ratios with A dwarfs (and propagated through HR 6348 as an intermediate calibrator) offer the best solution at wavelengths below 20 μm, to the red, fringing limits the fidelity of the IRS data to $\sim$1%.

6. THE K GIANTS

6.1. Spectra

Figures 7–12 plot the spectra from the IRS of all 33 of our K giants in Rayleigh–Jeans units, organized by modified spectral class (as defined in Section 6.3). For each spectral subclass, a prototype is overplotted in all panels for comparison. This prototype is usually one of the spectra we observed repeatedly as a standard, but we have no such standard for K2 and K3.

HR 6348 is the prototype for K0. It and HR 6606, the other well-observed source in this group, are virtually identical out to 20 μm. The deviations in HD 41371 may be attributable to pointing errors and the resulting throughput variations in the slit (SPITE, see Section 4.1), as this source was only observed once. More generally, the fewer times a spectrum was observed, the more likely these throughput errors will affect the shape of the spectrum especially in SL. This effect can be seen in several spectra in these and other figures. For sources observed many times (see the last column of Table 2), individual pointing deviations average out and the shape of the spectrum becomes more reliable.

HR 7341 is the prototype for K1. The variations among the spectra are more noticeable than for K0. HD 156061 stands out with its strong red excess, possibly from a debris disk, which would be unusual for a K giant. We discuss this excess further in Section 9.1 below.

None of the K2 giants were observed more than four times, and the quality of the spectra reflect that, with strong fringing in LL1 and more obvious noise. HD 50160 is the prototype because it was observed more than the others and has a better behaved spectrum. It also has the strongest SiO absorption, which is consistent with its redder B–V color (Section 6.3 below).

The K3 giants also show noisy spectra with LL1 fringing, due to the relatively low number of observations. HD 214873 is the prototype for the group because it has the best behaved spectrum, even though it was observed only once. Because this

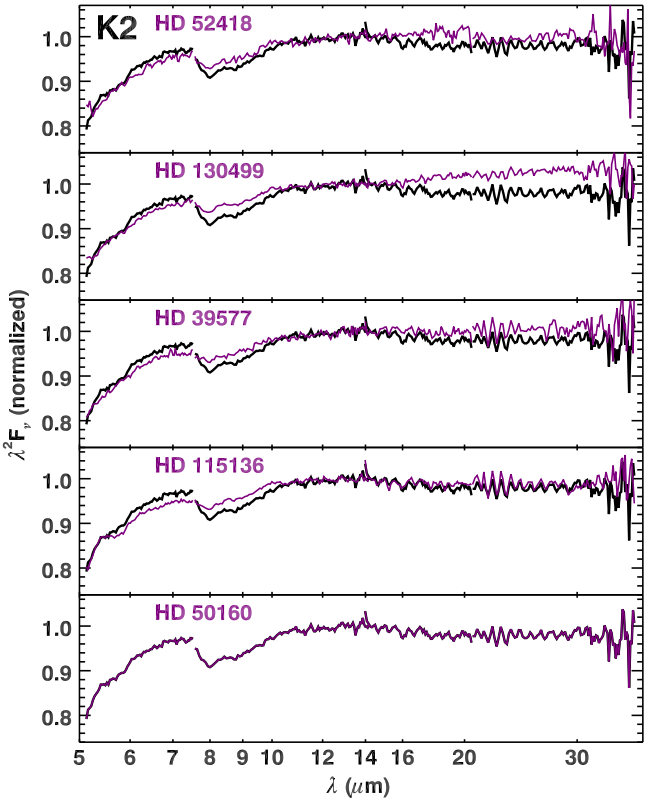

Figure 9. IRS spectra of the K2 giants, plotted as in Figure 7. HD 50160 appears in each panel in black; is not an ideal prototype due to the fringing in LL1, but none of the other spectra are as suitable.

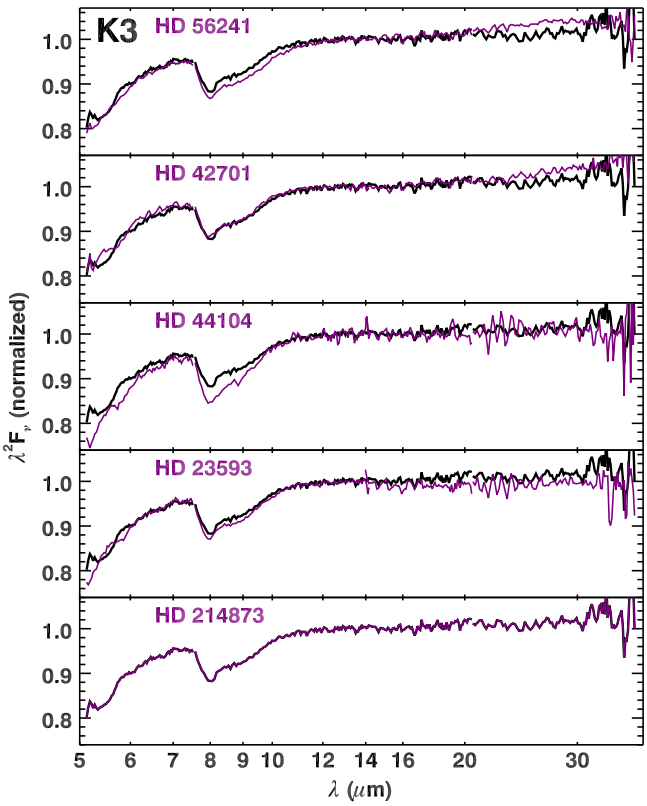

Figure 10. IRS spectra of the K3 giants, plotted as in Figure 7. The prototype here is HD 214873, although it was observed only once; it appears in black in each panel. The structure in its spectrum at 5.2 μm is probably not real.

observation came in Campaign P, before normal science operations had even begun, our confidence in the calibration is limited, making it likely that the structure at 5.2 μm is not real. The other spectra show considerable variation in the strength of the SiO band, with HD 42701 and HD 44104 representing the extremes. Two spectra, HD 56241 and HD 42701, show a measurable red excess compared to HD 214873.

HD 166780 is the prototype for the K4 giants. This group exhibits a range of SiO absorption strengths, with HD 166780 showing the weakest band. The fringing in LL1 (past 20 μm) is quite noticeable in some of the spectra and can be distinguished from the OH band structure from 14 to 18 μm.

The prototype for the K5 giants is HD 173511. As with K4, these spectra show a variety of SiO band strengths, OH band structure in LL2, and fringing in LL1.

6.2. Measuring the SiO Absorption Band

To measure the equivalent width of the SiO absorption band at 8 μm in the K giants, it is necessary to also determine the interstellar extinction and the temperature of the continuum simultaneously. Using the optical photometry of the stars to determine A_v proved unfeasible, because the reddening vector in *UBV* color space follows too closely the effect of changing temperature for K giants. Sources with high extinction have absorption from interstellar silicate dust at 10 μm, which tends to extend the SiO absorption to longer wavelengths and adds to its apparent equivalent width.

We fitted the SiO band strength, A_v, and continuum temperature simultaneously, minimizing the χ^2 residuals from 6.8 to 11.2 μm. Our A_v estimates are based on the local silicate extinction profiles by Chiar & Tielens (2006). We determined the continuum temperature by forcing an Engelke function through the spectral continuum in the vicinity of 12 μm and at ~6.5–7.0 μm.

For the purposes of determining χ^2, we used a mean SiO profile constructed from the SWS spectra of eight K and M giants (recalibrated by Engelke et al. 2006). Table 1 lists 10 K and M giants for which recalibrated SWS spectra exist. We used all except β UMi, which has no measurable SiO absorption, and β Peg, which Engelke et al. (2006) reject as a trustworthy standard due to its photometric variability. Figure 13 presents the eight resulting SiO profiles, fitted with Engelke functions using the temperatures determined by Engelke (1992). The spectra do show some variation in the shape of the SiO profile, but no systematic dependence with spectral class, leading us to take the mean of all eight to use for our IRS spectra.

While iterating, our minimum step size was 0.01 mag for A_v and 50 K for T. Table 5 presents the results. The fitted continuum temperatures in Table 5 have limited physical significance because they are sensitive to errors in the slope of the spectrum in the SL module commonly produced by the typical pointing errors (SPITE, Section 4.1).

6.3. SiO, Color, and Spectral Class

One of our objectives was to probe how well the optical spectral class of a star predicted the SiO band strength in the mid-infrared. This question drove our desire to observe several targets at each subclass, giving us a sample large enough to compare variations in SiO band strength from one subclass to

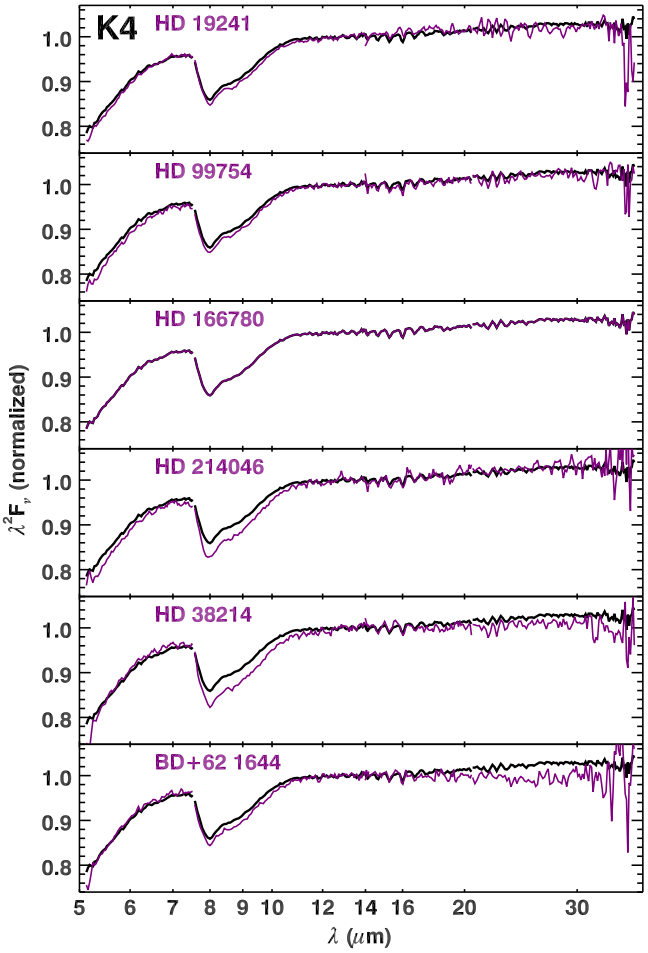

Figure 11. IRS spectra of the K4 giants, plotted as in Figure 7. HD 166780 is the prototype, overplotted in black in each panel.

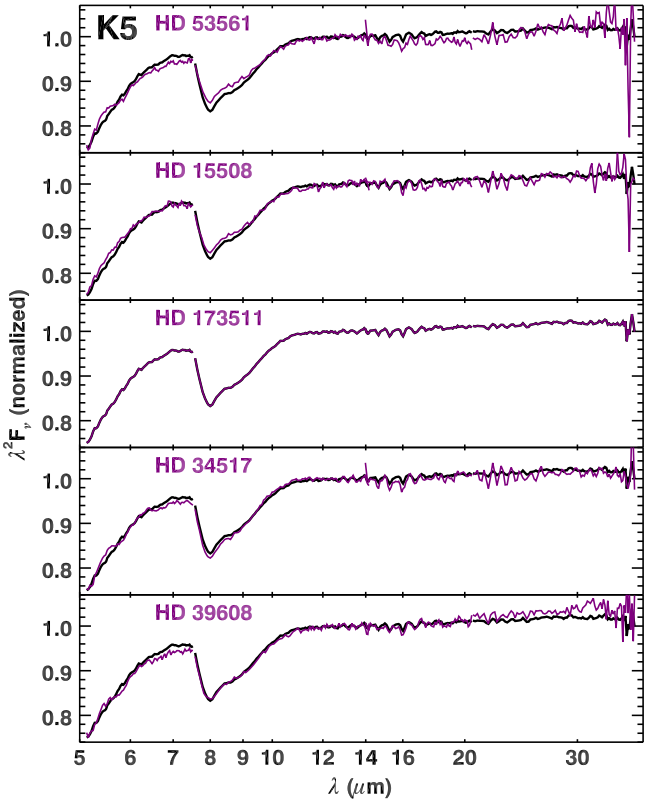

Figure 12. IRS spectra of the K5 giants, plotted as in Figure 7. HD 173511 is the prototype, overplotted in each panel in black.

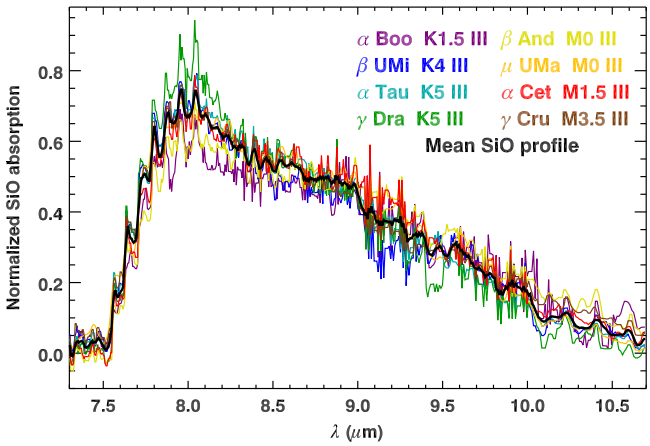

Figure 13. Constructing a mean SiO absorption profile from the SWS spectra of several standard stars. We have median-smoothed the spectra before plotting to reduce the noise and reveal more of the spectral details. While the shape of the SiO band varies from source to source, no dependence with spectral class is apparent.

the next, and also within a given subclass. Discrepancies in classifications from different spectroscopists can lead to some amibiguity when deciding which of our observed stars belong to which subclass.

Prior to launch, M. Cohen delivered spectral templates to the Cornell team for most of the planned standards. The spectral subclass used to determine the template depended more on how well the photometry for the target in question fit the available templates, leading to some reclassifications and further ambiguity.

We have modified the optical spectral classes based on the dereddened $(B–V)_0$ colors in the right-most column in Table 5. These are based on the interstellar extinction A_V determined in Section 6.2 and a $B–V$ color generated from photometry in the Tycho 2 catalog as described in Section 7. We require that the sequence from K0 to K5 increases monotonically with $(B–V)_0$, and we have defined the breaks between subclasses to minimize the changes required from the literature. This approach generally works, but two issues stand out. First, most of the K2 giants in our sample have colors close to K1, except for HD 50160, which is the single source in the sizable gap between HD 155136 (K2) and HD 56241 (K3). Second, the colors of K4 and K5 giants form a smooth continuum, forcing a fairly arbitrary separation. Placing the boundary between BD+62 1644 (K4) and HD 53561 (K5) minimizes changes to earlier spectral classifications. In all, we have changed 10 of 33 spectral classes from what appears in the literature. These have modified spectral classes in bold in Table 2.

Figure 14 shows how the equivalent width of the SiO absorption band depends on $B–V$ color. It also shows the effect of dereddening the $B–V$ color, based on the A_V values determined from fitting the SiO profile in the previous section. The crowding at K1–K2 and K4–K5 is readily apparent. The uneven spacing for the subclasses illustrates quite nicely the

Table 5
Observed SiO Measurements

Source	Fitted T (K)[a]	Fitted A_v (mag)	Equivalent Width SiO (μm)	$(B-V)_0$ (mag)
HD 41371	4600	0.28	0.045 ± 0.003	0.925 ± 0.010
HR 7042	3850	0.18	0.014 ± 0.005	0.935 ± 0.009
HD 51211	3400	0.11	0.027 ± 0.000	0.969 ± 0.009
HR 6606	4150	0.03	0.023 ± 0.003	1.006 ± 0.009
HR 6348	4300	0.02	0.025 ± 0.003	1.015 ± 0.009
HR 2712	3600	0.03	0.027 ± 0.010	1.030 ± 0.009
HR 1815	5350	0.17	0.045 ± 0.003	1.054 ± 0.009
HD 59239	4250	0.10	0.052 ± 0.008	1.061 ± 0.010
HD 156061	3100	0.36	0.053 ± 0.003	1.066 ± 0.010
HR 6790	3550	0.01	0.036 ± 0.010	1.072 ± 0.009
HD 39567	3350	0.12	0.070 ± 0.004	1.108 ± 0.011
HR 7341	4100	0.00	0.053 ± 0.004	1.126 ± 0.010
HD 52418	4150	0.00	0.052 ± 0.004	1.141 ± 0.010
HD 130499	3900	0.00	0.042 ± 0.005	1.152 ± 0.009
HD 39577	3600	0.00	0.051 ± 0.007	1.152 ± 0.011
HD 115136	3400	0.00	0.044 ± 0.004	1.155 ± 0.010
HD 50160	4900	0.03	0.111 ± 0.015	1.234 ± 0.011
HD 56241	3350	0.21	0.155 ± 0.013	1.321 ± 0.012
HD 42701	4000	0.00	0.131 ± 0.005	1.370 ± 0.009
HD 44104	3300	0.00	0.185 ± 0.004	1.385 ± 0.013
HD 23593	3750	0.05	0.156 ± 0.001	1.388 ± 0.010
HD 214873	3550	0.02	0.133 ± 0.003	1.389 ± 0.012
HD 19241	4000	0.02	0.196 ± 0.013	1.411 ± 0.011
HD 99754	3450	0.02	0.195 ± 0.006	1.419 ± 0.011
HD 166780	3900	0.00	0.171 ± 0.005	1.421 ± 0.011
HD 214046	3450	0.04	0.227 ± 0.017	1.446 ± 0.012
HD 38214	4150	0.18	0.245 ± 0.008	1.451 ± 0.019
BD+62 1644	4150	0.07	0.213 ± 0.006	1.451 ± 0.025
HD 53561	3450	0.00	0.169 ± 0.023	1.454 ± 0.014
HD 15508	3900	0.00	0.197 ± 0.007	1.455 ± 0.013
HD 173511	3900	0.00	0.218 ± 0.002	1.467 ± 0.011
HD 34517	3250	0.00	0.222 ± 0.012	1.557 ± 0.012
HD 39608	3300	0.00	0.208 ± 0.003	1.557 ± 0.012

Note.
[a] Temperature of fitted Engelke function, but this quantity has limited physical significance. See Section 6.2.

difficulty in equating spectral classes determined spectroscopically with the photometry.

Figure 15 plots the equivalent width of the SiO band as a function of both the modified spectral class and $(B–V)_0$ color. The Cohen composites are β UMi (K0), α Boo (K1.5), α Hya (K3), and α Tau (K5). The points for K1, K2, and K4 are based on weighted means of the above four sources. The averaged IRS data are for each modified spectral subclass. We fitted quadratics to the Cohen composites and averaged IRS data and plotted these as well. The apparent difference between the fits in the top and bottom panel is due to the differences in colors between the sources used for the Cohen composites and in our sample. The K1.5 giant α Boo is redder than all but one of the K2 giants in our sample, and the $B–V$ color for the K2 composite is closer to our K3 sources. The bottom panel shows that plotting versus color instead of spectral class eliminates this problem, and the resulting distributions are virtually identical.

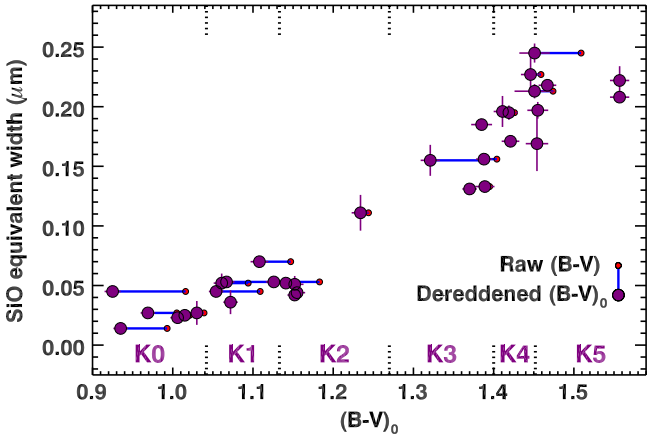

Figure 14. Equivalent width of the SiO absorption band at 8 μm as a function of $B–V$ color. The larger circles plot $(B–V)_0$, while the horizontal lines and smaller circles depict the raw $B–V$ colors.

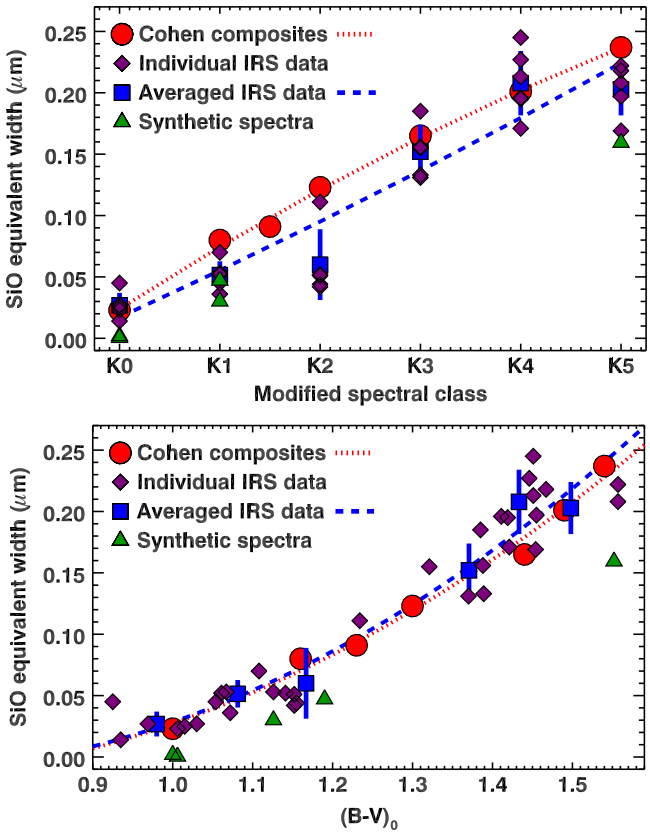

Figure 15. Equivalent width of the SiO band as a function of modified spectral class (top) and dereddened $B–V$ (bottom). The Cohen composite spectra are plotted as red circles, while the individual IRS sources appear as blue diamonds. The average for each subclass are plotted as purple squares, along with their standard deviations. The dotted and dashed lines are quadratics fitted to the Cohen composites and averaged IRS data, respectively.

We can also measure the SiO band strength in the synthetic spectra of the five giants considered by Decin et al. (2004).[18] These sources include two of the low-resolution IRS standards examined in Section 5.3 (HR 6606 and HR 7341), two bright K

[18] This group includes two stars classified in the literature as G9 III, but we will consider them as part of the K-giant sample.

Table 6
Bright K Giants

Source	HR	Sp. Type	Reference[a]	$(B-V)_0$[b]	Sp. Class from Color[c]	F_ν at 12 μm (Jy)[d]	IRS Obs.	Synthetic Spectrum
δ Dra	7310	G9 III	many	1.000	**K0**	14.6	4	Y
42 Dra	6945	K2 III	many	1.182	**K1**	5.1	2	
ξ Dra	6688	K2 III	many	1.190	**K1**	11.7	44[e]	Y
HR 5755	5755	K5 III	SIMBAD	1.447	**K4**	3.6	2	
γ Dra	6705	K5 III	many	1.552	K5	106.9	⋯	Y
HR 420	420	K5 III	MSS-75	1.548	K5	5.0	2	

Notes.
[a] MSS-75 = Michigan catalog, vol. 1 (Houk & Cowley 1975), SIMBAD = in SIMBAD, but with no further references, many = many references given in SIMBAD, all of which agree.
[b] A_v assumed to be 0.
[c] Changes are in bold; see Section 6.3.
[d] Photometry from the *IRAS* PSC (Beichman et al. 1988) and color corrected by dividing by 1.45.
[e] Only 21 spectra coadded.

Table 7
Synthetic SiO Measurements

Source	Equivalent Width of SiO (μm)
δ Dra	0.0019
HR 6606	0.0004
HR 7341	0.0301
ξ Dra	0.0471
γ Dra	0.1594

giants observed in LL with the IRS (ξ Dra and δ Dra), and γ Dra, which served as the primary standard for the *ISO*/SWS, but was much too bright for the low-resolution IRS modules (it also appears in Table 6).

We have generated an optical B–V color for the bright giants in Table 6 as for the fainter giants in Table 5. The bright giants are close enough that we can assume $A_v = 0$. Modifying the spectral classes based on B–V would shift four of the six bright giants by one subclass, which points to a subtle disconnect between the temperatures of the different layers producing the continuum, atomic absorption lines, and molecular absorption bands.

Table 7 gives the SiO equivalent widths from the synthetic spectra, and Figure 15 compares them to the observed band strengths. In the top panel, we have used the modified spectral classes for the sources (in Tables 2 and 6). The synthetic data are always below the fitted polynomials and generally below the observed data. The B–V colors in the bottom panel are from Tables 5 and 6, and here all of the synthetic data are below the lower envelope defined by the observed data. These results build on the more qualitative comparisons made in Section 5.3. Previously, the best example of this disagreement was γ Dra (Price et al. 2002). The synthetic band is weaker than observed in spectra from the *ISO*/SWS (as can be seen in Figure 3 of Decin et al. 2004). While the differences in band strength are not dramatic, they are large enough to propagate an SiO emission artifact into the larger database if the synthetic spectra are used as truth spectra.

Figure 15 shows that $(B-V)_0$ is a better predictor of SiO band strength than spectral class. The reason may lie in what the spectral class and B–V color are measuring. For K giants, the determination of the spectral subclass is based on the relative strengths of atomic lines from metals. The B–V color measures the shape of the continuum, and it is strongly influenced by the H^- ion (Wildt 1939). Our results suggest that the H^- ion better traces the region in which the molecular bands arise than the metallic lines.

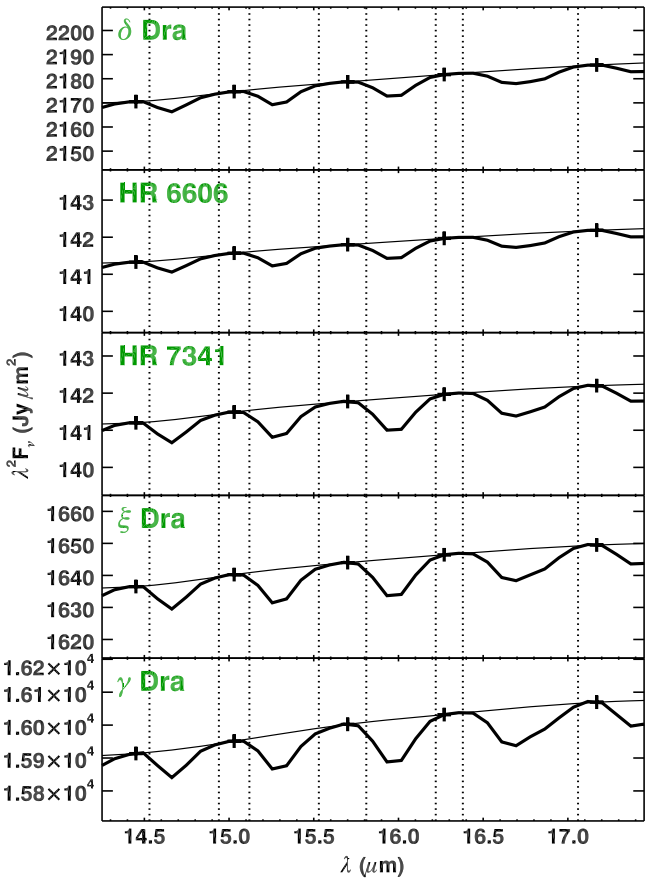

Figure 16. Extracting the four OH bands in the 14.5–17 μm region of the synthetic spectra of K giants by Decin et al. (2004), rebinned to the IRS resolution. The thicker lines trace the actual spectra, while the thinner lines trace the fitted splines, which run through the plus signs. The vertical dashed lines mark the wavelength limits for integrating the equivalent width of each band. All five panels have a vertical extent of 3.1% of the mean.

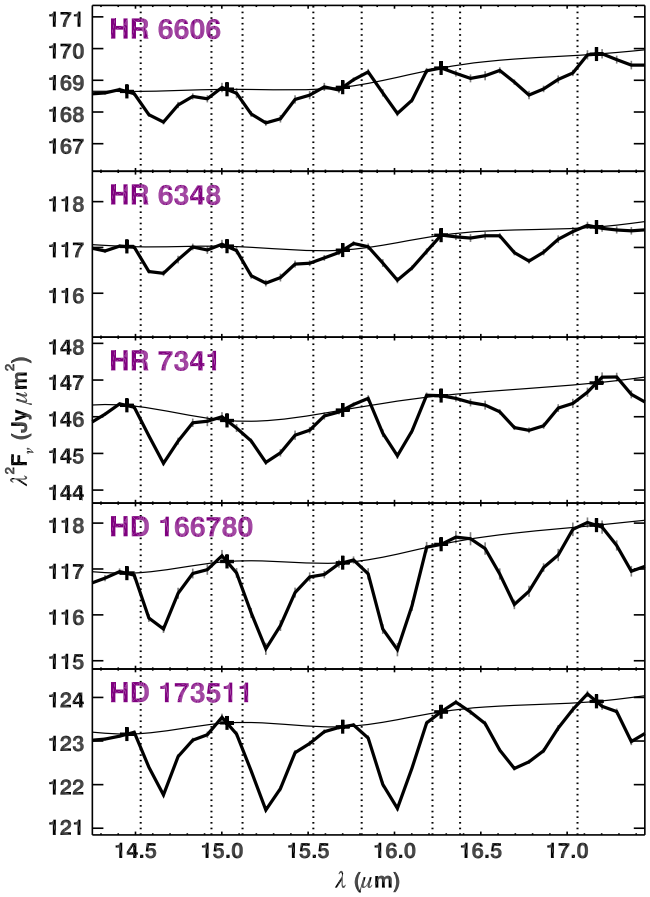

Figure 17. OH spectrum of the IRS low-resolution standards. Lines and symbols are defined as in Figure 16, and as before, the vertical range of each panel is 3.1% of the mean.

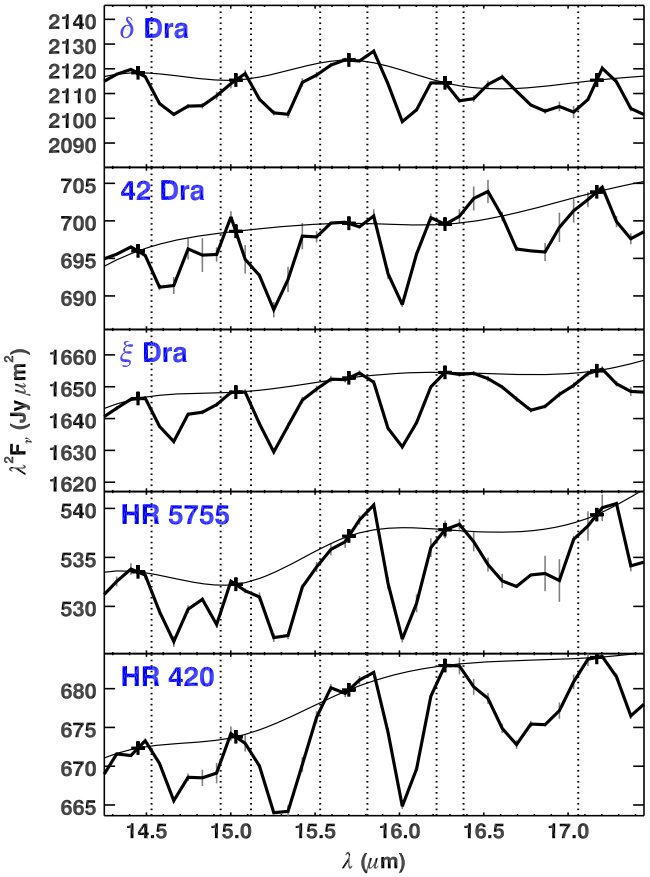

Figure 18. OH spectrum of the bright K giants observed with the IRS LL module. Lines, symbols, and vertical extent of the panels are as for Figures 16 and 17.

Table 8
OH Band Strengths

Source	Equivalent Width of Combined Bands (nm)	Relative Contribution from Bands at 14.7 μm	15.3 μm	16.0 μm	16.7 μm
		Synthetic Spectra			
δ Dra	3.12 ± ⋯	0.17 ± ⋯	0.25 ± ⋯	0.28 ± ⋯	0.31 ± ⋯
HR 6606	2.95 ± ⋯	0.16 ± ⋯	0.25 ± ⋯	0.28 ± ⋯	0.31 ± ⋯
HR 7341	5.60 ± ⋯	0.16 ± ⋯	0.24 ± ⋯	0.29 ± ⋯	0.32 ± ⋯
ξ Dra	6.43 ± ⋯	0.15 ± ⋯	0.24 ± ⋯	0.29 ± ⋯	0.32 ± ⋯
γ Dra	7.25 ± ⋯	0.14 ± ⋯	0.23 ± ⋯	0.30 ± ⋯	0.34 ± ⋯
		IRS Low-resolution Standards			
HR 6606	6.75 ± 0.43	0.20 ± 0.03	0.25 ± 0.04	0.13 ± 0.02	0.42 ± 0.04
HR 6348	6.27 ± 0.41	0.17 ± 0.03	0.33 ± 0.03	0.23 ± 0.03	0.27 ± 0.04
HR 7341	9.05 ± 0.40	0.20 ± 0.02	0.24 ± 0.02	0.18 ± 0.02	0.38 ± 0.03
HD 166780	13.92 ± 0.67	0.16 ± 0.02	0.31 ± 0.02	0.26 ± 0.02	0.27 ± 0.03
HD 173511	13.70 ± 0.31	0.16 ± 0.01	0.30 ± 0.01	0.26 ± 0.01	0.28 ± 0.01
		IRS Observations of Bright K Giants			
δ Dra	8.05 ± 0.33	0.30 ± 0.02	0.26 ± 0.03	0.19 ± 0.01	0.25 ± 0.01
42 Dra	10.06 ± 0.47	0.21 ± 0.03	0.37 ± 0.02	0.24 ± 0.02	0.18 ± 0.03
ξ Dra	10.17 ± 0.45	0.20 ± 0.02	0.25 ± 0.03	0.31 ± 0.02	0.23 ± 0.03
HR 5755	14.95 ± 0.63	0.20 ± 0.02	0.23 ± 0.02	0.24 ± 0.02	0.33 ± 0.02
HR 420	18.85 ± 0.61	0.14 ± 0.01	0.24 ± 0.02	0.26 ± 0.00	0.35 ± 0.03

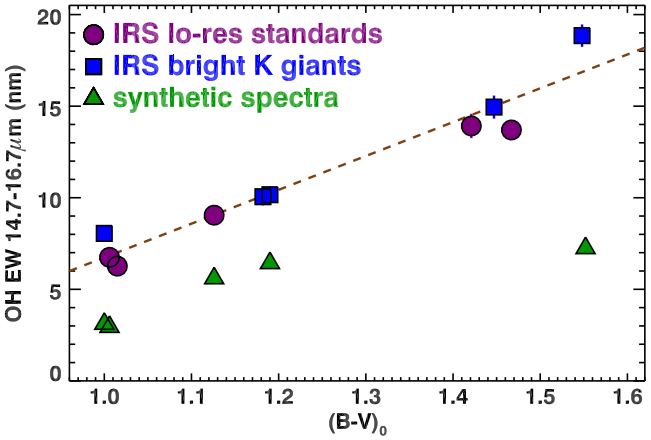

Figure 19. Sum of the equivalent width of the four OH bands between 14.5 and 17 μm, plotted as a function of $(B–V)_0$. The uncertainties are generally smaller than the symbols. The dashed line is a least-squares fit to the IRS data. The OH bands in the observed IRS spectra are consistently stronger than in the synthetic spectra, and the difference increases as the stars grow cooler.

6.4. OH Absorption

The spectral templates and synthetic spectra of K giants behave differently past $\sim$12 μm. The spectral templates assumed that the long-wavelength behavior of a giant could be modeled with an Engelke function, which falls off smoothly with increasing wavelength, while the synthetic spectra show corrugation from OH absorption bands, which can grow as strong as $\sim$1% in the 14–18 μm region.

The observed IRS spectra confirm the presence of OH band structure. To examine how the OH bands vary with effective temperature and compare to their predicted structure in the synthetic spectra, we focus on the spectral region where they are strongest, which is covered by LL2. In particular, we concentrate on the strongest four bands centered at 14.7, 15.3, 16.0, and 16.7 μm.

We base our analysis on the five K giants observed repeatedly by the IRS in both SL and LL (HR 6348, HD 166780, HD 173511, HR 6606, and HR 7341; see Sections 4.3, 5.2, and 5.3) and five brighter K giants observed with LL, but not SL. These include ξ Dra, which served as our high-resolution standard, and four other IRS targets listed in Table 6, which gives their basic optical and infrared properties. With the exception of ξ Dra, these stars were observed only 2–4 times, but they are bright enough to produce spectra with sufficient S/N for analysis of the OH bands.

Figure 16 presents the LL2 portion of the synthetic spectra and illustrates how we fit a spline to the continuum and measured the equivalent width of the OH bands. The available low-resolution synthetic spectra were released before multiple changes to the wavelength calibration. To match the currently used wavelength grid and resolution, we regridded the spectra, using a Gaussian convolution. A comparison of Figure 16 to the actual IRS measurements of the low-resolution standards in Figure 17 and the brighter giants in Figure 18 shows that we are comparing spectra with similar resolutions. The dotted vertical lines in the figures mark the wavelength ranges over which we integrated the equivalent widths; they are fixed for all of the spectra, despite a slight shift between the synthetic and actual

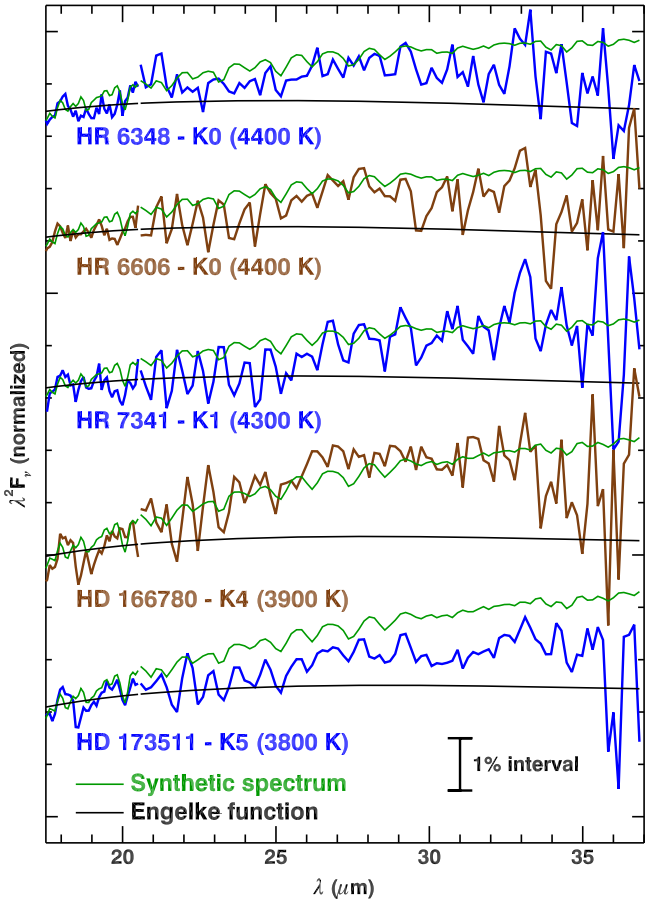

Figure 20. Comparison of the shape of our low-resolution spectra at longer wavelengths to Engelke functions and synthetic spectra. The spectrum of HR 6348 is the truth spectrum (Section 4.3); the others are coadded spectra. The synthetic spectra and Engelke functions are normalized to match the IRS data at 17.5–18.5 μm. The synthetic spectra are for HR 6606 (K0), HR 7341 (K1), and γ Dra (K4–5). The temperatures of the Engelke functions are given in parentheses next to the adopted spectral classes of each star. A 1% interval in the data is shown below the bottom spectrum. The IRS data are more consistent with the long-wavelength shape of the synthetic spectra than the Engelke functions, but enough variation exists to prevent any firm conclusions.

spectra. These shifts are too small to account for the differences between the two sets of data.

Table 8 presents the total equivalent widths of the four bands (in nm) and the individual contributions (as a fraction of the total). In order to propagate errors to estimate the uncertainty in the equivalent widths, we have attempted to remove the photometric component from the uncertainties in the spectra. These arise because of fluctuations in slit throughput from one spectrum to the next and dominate the spectroscopic (or point-to-point) uncertainties.

Figure 19 plots the total measured OH equivalent width as a function of $(B–V)_0$ for the synthetic spectra, the low-resolution standards, and the brighter K giants. Both sets of giants observed with the IRS show the same relation of steadily increasing equivalent width as a function of $B–V$ color. The line fitted in the figure gives

$$EW\,(\mathrm{nm}) = -11.7 + 18.5(B - V)_0. \quad (2)$$

The synthetic spectra show consistently weaker OH bands. For the four spectra with $B–V < 1.2$ (or spectral classes earlier than K3), the relation could be described with a similar slope, but a lower y-intercept, with a mean shift of -3.7 ± 0.2 nm.

Table 9
K Giant Photometry

Target	B_T	V_T	V_0	F_{22} (mJy)[a]	$V-$ [22]
HD 41371	8.381 ± 0.016	7.204 ± 0.010	6.811	116.5	2.194
HR 7042	7.349 ± 0.015	6.201 ± 0.010	5.911	(233.0)	2.046
HD 51211	8.069 ± 0.015	6.906 ± 0.010	6.685	143.2	2.291
HR 6606	7.159 ± 0.015	5.982 ± 0.009	5.839	341.3	2.389
HR 6348	7.440 ± 0.015	6.256 ± 0.010	6.123	234.7	2.266
HR 2712	7.797 ± 0.015	6.590 ± 0.009	6.445	201.3	2.421
HR 1815	7.929 ± 0.015	6.632 ± 0.009	6.339	220.9	2.416
HD 59239	8.135 ± 0.016	6.858 ± 0.010	6.637	175.8	2.466
HD 156061	8.680 ± 0.017	7.288 ± 0.011	6.796	202.8	2.780
HR 6790	7.667 ± 0.015	6.414 ± 0.010	6.285	236.7	2.437
HD 39567	9.049 ± 0.018	7.704 ± 0.011	7.456	90.4	2.563
HR 7341	7.760 ± 0.016	6.442 ± 0.010	6.317	293.1	2.701
HD 52418	8.341 ± 0.016	7.003 ± 0.010	6.876	172.8	2.686
HD 130499	8.074 ± 0.015	6.722 ± 0.010	6.594	218.3	2.658
HD 39577	8.584 ± 0.017	7.232 ± 0.010	7.104	118.1	2.501
HD 115136	7.994 ± 0.016	6.639 ± 0.010	6.510	229.6	2.629
HD 50160	9.190 ± 0.018	7.720 ± 0.011	7.550	109.3	2.863
HD 56241	9.472 ± 0.019	7.816 ± 0.011	7.446	172.1	3.252
HD 42701	8.467 ± 0.015	6.836 ± 0.010	6.679	(338.4)	3.219
HD 44104	9.470 ± 0.020	7.819 ± 0.011	7.659	155.3	3.354
HD 23593	9.200 ± 0.017	7.525 ± 0.011	7.313	216.4	3.367
HD 214873	8.579 ± 0.018	6.915 ± 0.010	6.734	(343.4)	3.290
HD 19241	8.948 ± 0.017	7.256 ± 0.010	7.072	256.0	3.309
HD 99754	9.111 ± 0.017	7.408 ± 0.010	7.222	230.5	3.346
HD 166780	9.198 ± 0.018	7.501 ± 0.011	7.336	237.0	3.489
HD 214046	9.456 ± 0.019	7.710 ± 0.011	7.499	202.8	3.483
HD 38214	10.083 ± 0.027	8.273 ± 0.012	7.914	149.2	3.565
BD+62 1644	10.549 ± 0.035	8.784 ± 0.014	8.541	77.4	3.479
HD 53561	9.335 ± 0.022	7.596 ± 0.012	7.426	211.2	3.454
HD 15508	9.552 ± 0.020	7.811 ± 0.011	7.641	172.1	3.447
HD 173511	9.156 ± 0.018	7.400 ± 0.011	7.228	247.1	3.427
HD 34517	9.248 ± 0.018	7.376 ± 0.010	7.188	(387.5)	3.876
HD 39608	9.413 ± 0.019	7.542 ± 0.011	7.355	(296.6)	3.752

Note.
[a] Values in parentheses are determined from the spectra.

For all four, we are comparing synthetic spectra and observed IRS spectra of the same sources. If the one point for γ Dra at $B–V = 1.55$ is characteristic of the behavior at later spectral classes, then the slope of the OH dependence in the synthetic spectra decreases for redder sources, while the IRS data are consistent with an unchanging slope at all $B–V$ colors.

Van Malderen et al. (2004) compared the strength of the OH bands in this wavelength range as observed by the *ISO*/SWS for several of the giants listed in Table 1 with synthetic spectra, and they also found that the observed bands were stronger than predicted by the models. High-resolution spectroscopy of OH lines in α Boo by Ryde et al. (2002) uncovered a similar problem. They found that a cooler upper atmosphere in the model produced stronger OH lines and better reproduced the observations. Van Malderen et al. (2004) noted that the rising opacity of the H^- ion with wavelength would push the continuum and the region probed by the molecular bands to larger radii at longer wavelengths. This in turn would produce the need for lower temperatures and stronger bands. It also explains how synthetic spectra which fit the observed data so well at wavelengths below 6 μm (e.g., Decin et al. 2003a; 2003b) can be less successful at longer wavelengths. Decin & Eriksson (2007) noted that using different absorption coefficients for H^- in their models changed the SiO band depth by 3%, reinforcing the importance of this ion to the emergent spectrum.

The power of the synthetic spectra lies in their prediction of the presence of the OH bands. Early spectral templates used by us relied on smooth Engelke functions in this wavelength range, even though van Malderen et al. (2004) and Decin et al. (2004) had shown that these bands were present in the spectra, the latter using IRS data. It is unfortunate that the Cornell calibration did not reflect this fact until later in the mission.

6.5. Engelke Functions

Figure 20 compares the IRS data at longer wavelengths to Engelke functions and synthetic spectra. The temperatures of the Engelke functions are based on the temperatures of the adopted spectral classes. We do not have synthetic spectra for

Table 10
A Dwarf Photometry

Target	B_T	V_T	V_0[a]	$(B–V)_0$[a]	F_{22} (mJy)[b]	$V-$ [22]
HR 1014	6.203 ± 0.014	6.041 ± 0.009	6.022	0.142	(41.7)	0.290
ν Tau	3.939 ± 0.014	3.888 ± 0.009	3.882	0.040	234.5	0.024
η^1 Dor	5.681 ± 0.014	5.688 ± 0.009	5.690	–0.012	(38.9)	–0.120
HD 46190	6.709 ± 0.014	6.618 ± 0.010	6.607	0.076	(26.2)	0.368
21 Lyn	4.594 ± 0.014	4.607 ± 0.009	4.610	–0.018	114.5	–0.027
26 UMa	4.515 ± 0.014	4.468 ± 0.009	4.463	0.036	153.4	0.144
HR 4138	4.766 ± 0.014	4.715 ± 0.009	4.709	0.040	121.4	0.137
τ Cen	3.913 ± 0.014	3.848 ± 0.009	3.841	0.053	273.4	0.149
ξ^1 Cen	4.854 ± 0.014	4.828 ± 0.009	4.826	0.017	108.4	0.130
HR 5467	5.818 ± 0.014	5.816 ± 0.009	5.817	–0.004	37.4	–0.034
HR 5949	6.259 ± 0.014	6.299 ± 0.010	6.305	–0.041	(28.4)	0.154
δ UMi	4.380 ± 0.014	4.340 ± 0.009	4.336	0.030	156.8	0.041
HD 163466	7.085 ± 0.015	6.875 ± 0.010	6.850	0.188	23.5	0.495
HR 7018	5.671 ± 0.014	5.718 ± 0.009	5.725	–0.047	37.1	–0.135
λ Tel	4.775 ± 0.014	4.829 ± 0.009	4.837	–0.054	86.6	–0.102
HD 165459	7.020 ± 0.015	6.875 ± 0.010	6.858	0.126	(27.0)	0.652
29 Vul	4.774 ± 0.014	4.798 ± 0.009	4.802	–0.027	91.1	–0.082
ϵ Aqr	3.769 ± 0.014	3.758 ± 0.009	3.758	0.004	265.8	0.036
μ PsA	4.572 ± 0.014	4.502 ± 0.009	4.494	0.057	151.3	0.160
α Lac	3.784 ± 0.014	3.758 ± 0.009	3.756	0.017	252.0	–0.024

[a] Assumed to be unreddened.
[b] Values in parentheses are determined from the spectra, after correcting for the 24 μm dip.

Table 11
Photometric Transformations and Color Relations

Relation	Range	Polynomial Coefficients			
$B-V$ vs. B_T-V_T	1.10–1.90	0.099	0.779		
$B-V$ vs. B_T-V_T	–0.10–0.25	–0.006	0.890	0.155	
$V-V_T$ vs. B_T-V_T	all	0.001	–0.013	0.055	–0.020
$V-$[22] vs. $B–V$	all	–0.008	2.380		
$V-$[22] vs. $B–V$	0.90–1.60	–0.240	2.561		
$V-$[22] vs. $B–V$	–0.06–0.20	–0.004	2.737		

all five sources, so we used the synthetic spectrum of HR 6606 for both it and HR 6348, while for HD 166780 and HD 173511, we used γ Dra. Both the synthetic spectra and Engelke function are scaled to the mean of the IRS data between 17.5 and 18.5 μm.

The corrugation in the LL1 spectra of HR 6606, HR 7341, and HD 166780 (to the red of 20.5 μm) is most likely due to fringing, but in the spectrum of HD 173511, the period and phase track the OH band structure surprisingly well. The difference in band strength compared to the synthetic spectrum roughly matches that measured in LL2 (Section 6.4).

The differences between the shape of the synthetic spectra and the Engelke functions are only ~1% from 17.5 to ~35 μm, and it is impressive that the IRS data are generally between them. The IRS data for HD 166780 follow the shape of the synthetic spectrum for all wavelengths below ~33 μm. Past ~30 μm, the data quickly become less trustworthy due to decreasing signal from the stars and responsivity in the Si:Sb detectors. For HR 6606 and HR 7341, the data diverge from the Engelke functions at ~25 μm and follow the synthetic spectra to ~33 μm. The IRS data for HR 6348 are more ambiguous, although they are generally closer to the synthetic spectrum. If we follow the continuum between OH bands in HD 173511, the spectrum generally stays right between the two. Thus, three of the spectra are more consistent with the shape of the synthetic spectrum, and none are more consistent with the shape of the Engelke function. Perhaps the firmest conclusion to be drawn is that the differences between the shapes of the synthetic spectra and the corresponding Engelke functions at these wavelengths are within ~1%.

7. PHOTOMETRY

Tables 9 and 10 present the optical and 22 μm PU photometry for our sample. The Tycho data are from the Tycho 2 catalog (Hog et al. 2000). Table 11 gives the transformations to convert to Johnson B and V, which we derived using data presented by Bessell (2000, Table 2). The K giants lie in the range $1.10 \leqslant B_T - V_T \leqslant 1.90$, and they follow a linear relation with $B–V$. The A dwarfs lie in the range $-0.10 \leqslant B_T - V_T \leqslant 0.25$, and for these a quadratic was necessary to transform to $B–V$. Bessell (2000) found that a cubic could fit $V - V_T$ as a function of $B_T - V_T$ for all colors.

We found no evidence of interstellar extinction in the IRS spectra of the A dwarfs, which is consistent with their close distances compared to the K giants. Consequently, we have used their $(B - V)$ colors and V magnitudes without correction. The V_0 magnitudes for the K giants in Table 9 are based on the extinctions in Table 5.

The Red PU photometry is labeled as F_{22} in Tables 9 and 10. The photometry for HR 7018 differs slightly from the value given by Sloan & Ludovici (2011b) because it adds seven observations late in the cryogenic mission not included earlier.

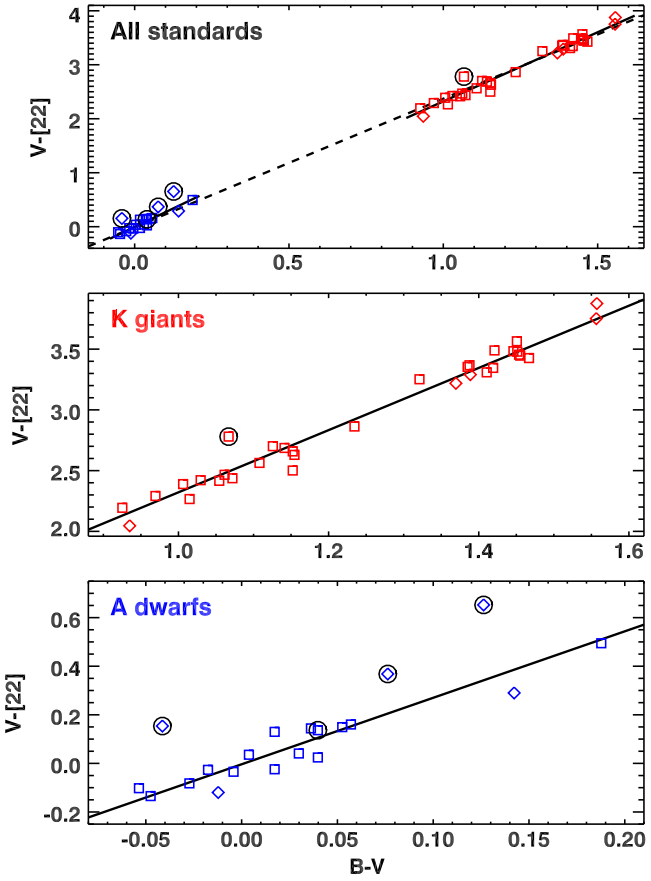

Figure 21. $V-[22]$ as a function of $B–V$. The top panel presents the data for all standards and the fitted lines. The dashed line is fitted to all of the data (after excluding outliers), while the solid line segments are fitted to the K giants and A dwarfs separately. Squares depict sources with Red PU photometry, while diamonds depict sources where [22] is based on the spectra. Data with possible debris disks are circled. The bottom two panels zoom in on the K giants and A dwarfs. The vertical scale of the A dwarfs in the bottom panel is half that of the K giants.

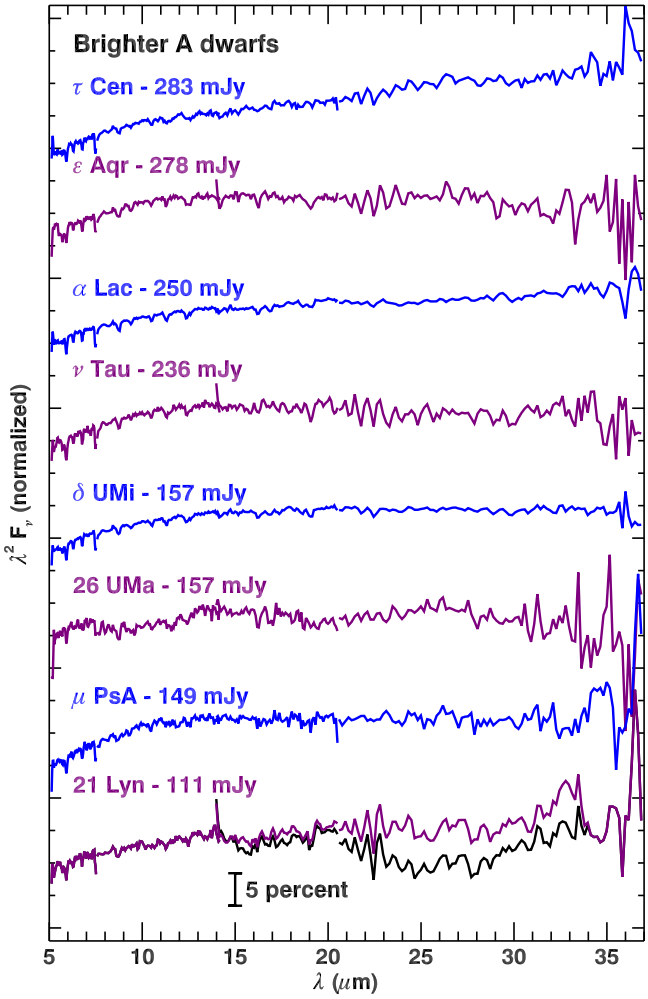

Figure 22. IRS spectra of the brighter A dwarfs observed as standards, plotted in Rayleigh–Jeans units. The spectrum of 21 Lyn has been corrected for the 24 μm dip, with the uncorrected spectrum shown in black. The flux densities given after the names of the sources are the values at 22.35 μm, as measured from the (corrected) spectra.

To convert to a magnitude, we have assumed a zero-magnitude flux density of 8.19 Jy at 22.35 μm, scaled from 7.30 Jy at 23.675 μm for MIPS-24.

Values for F_{22} in parentheses are for sources with no available photometry; instead, we estimated F_{22} from the spectra in a 1 μm window centered on 22.35 μm. For the A dwarfs, when the photometry is estimated from the spectra, it is *after* correcting for the 24 μm dip seen in some faint spectra, as described below (Section 8).

Table 11 includes linear relations of $V-[22]$ on $B–V$ fitted to all of our standards, along with separate relations for the K giants and A dwarfs. All of the lines are based on least-square fitting in two passes, with the second pass excluding data more than 0.10 mag from the line fitted in the first pass.

Figure 21 illustrates the dependence of $V-[22]$ on $B–V$ for the different samples. It is somewhat surprising that a single line fits all of the data as well as it does. The differences in the two lines fitted separately to the A dwarfs and K giants suggests that a cubic might fit all colors even better, but with no data for spectral classes F or G, we will just consider the separately fitted lines.

We have already noted the red excess in HD 156051 suggestive of a debris disk. Four of the A dwarfs also show possible debris disks. Figure 21 circles those data; they account for the worst outliers from the fitted lines. Excluding these five sources, we find a standard deviation of 0.073 mag about the fitted line for K giants and 0.053 mag for the A dwarfs. Both groups behave well.

The y-intercept of the relation between $B–V$ and $V-[22]$ for the A dwarfs is −0.0036, close to the expected value of zero and smaller than the standard deviation (0.053) and uncertainty in the mean (0.013). This result verifies that the MIPS calibration at 24 μm (Rieke et al. 2008) is consistent with the expected behavior of an A0 dwarf.

8. THE A DWARFS

Our sample of calibrators includes 20 A dwarfs. Their hotter effective temperatures make them easier to model and thus potentially better standards than K giants. However, they are far less common in the bright infrared sky, and their spectral properties have proven to be full of surprises. Eggen (1984) quotes W. P. Bidelman: "I do not know, nor have I ever seen, a normal A0 star."

Vega is a case in point. *IRAS* discovered a previously unsuspected debris disk (Aumann et al. 1984). Its narrow absorption lines arise from a pole-on configuration, as first

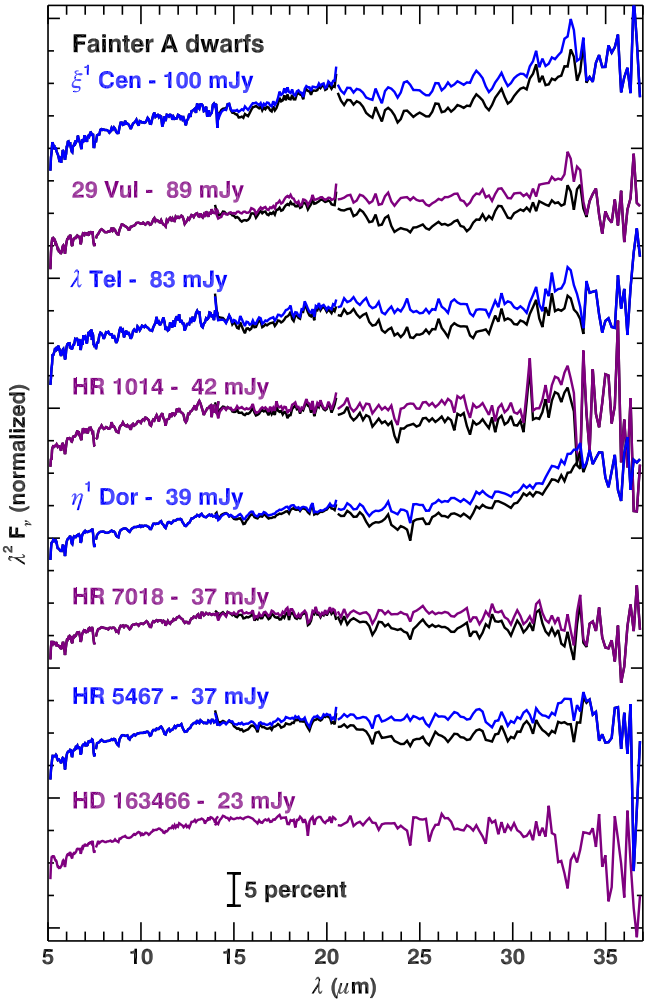

Figure 23. IRS spectra of the fainter A dwarfs observed as standards, plotted in Rayleigh–Jeans units. Traces and flux densities are as described in Figure 22.

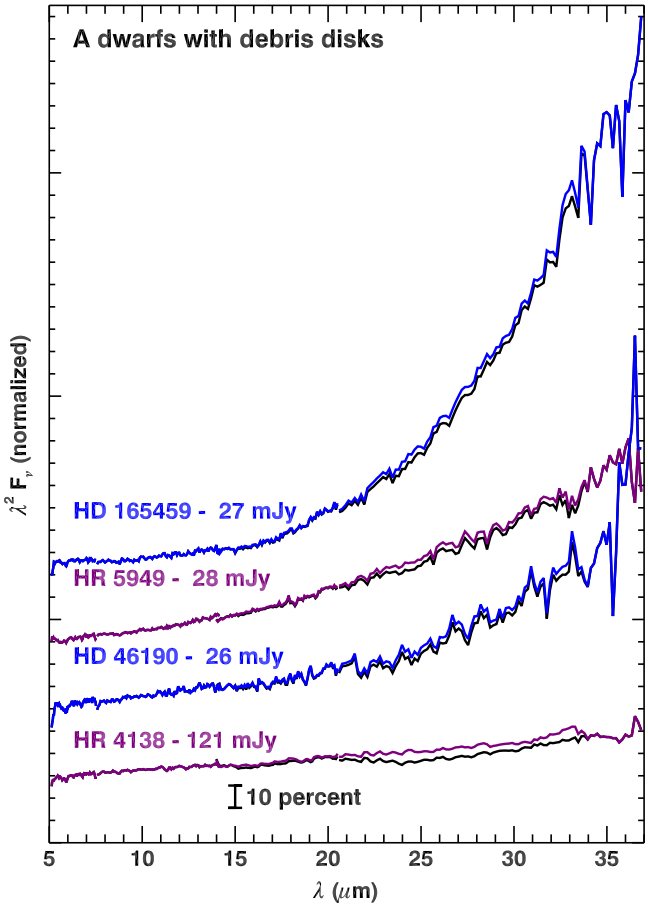

Figure 24. IRS spectra of the A dwarfs with excesses from possible debris disks, plotted in Rayleigh–Jeans units. Traces and flux densities are as described in Figure 22.

speculated by Gray (1985). Later work substantiates this scenario. We are seeing a fast rotator pole-on, leading to a range of effective temperatures across the disk of the star (Hill et al. 2010). It is rather ironic that Vega originally defined zero magnitude in most photometric systems.

While we used the available infrared photometry to select against obvious debris disks, we were still concerned that contamination from debris disks, binarity, or rotation and inclination effects might limit the utility of any star as a standard. Thus we observed many candidates for standards.

Figures 22 and 23 present the spectra of the A dwarfs observed as potential IRS standards, ordered by their brightness at 22 μm, while Figure 24 segregrates the four spectra showing red excesses from possible debris disks. Several others show fainter red excesses. We have already described α Lac as one example. These spectra are considered in Section 9.1 below.

Most of the fainter spectra suffer from an artifact known as the 24 μm dip, as can be seen in Figure 23. Our spectra show an impact in both LL2 and LL1, with the apparent detector output pushed down slightly at $\sim$15–18 μm and more significantly at $\sim$22–30 μm. An apparent upward cusp results at $\sim$19–20 μm.

To correct this artifact, we follow the method of Sloan et al. (2004), who first identified the problem when investigating the cool red excess around HD 46190. We have assumed that HR 5467 and HR 7018 should have shapes in LL2 and LL1 identical to those in δ UMi. We averaged their spectra, divided by δ UMi, normalized the result, and smoothed it. Due to the degrading S/N at longer wavelengths, we set the correction = 1 past 34 μm. To apply the correction to a given spectrum, we use the ratio of spectral emission at 24–25 μm to 19–20 μm (in Rayleigh–Jeans units) to estimate the strength of the 24 μm dip and scale the correction accordingly. For the four A dwarfs with possible debris disks, we use spectra with similar brightnesses to estimate the scaling, but as Figure 24 shows, the effect is only noticeable for HR 4138, which has the weakest excess of the four.

We assumed that the strength of the artifact depends on the brightness of the spectrum for the debris-disk candidates, which is disputable. For example, the faintest of our A dwarfs, HD 163466, shows no sign of the 24 μm dip. Except for this one source, all of the A dwarfs with $F_{22}<$ 115 mJy require a correction, but the two K giants fainter than this limit (HD 39567 and BD+62 1644) show no convincing evidence of the artifact (see Figures 8 and 11).[19] Nor do the two K giants in the 115–120 mJy range (HD 41371 and HD 39577; Figures 7 and 9).

Early in the mission, we found that some of the A dwarfs were brighter in the infrared than expected based on the

[19] BD+62 1644 does show a small deficit in LL1, but no cusp at $\sim$20 μm.

Table 12
Stellar Properties of Candidate Debris Disks

Source	Parallax (mas)	T_* (K)	BC (mag)	R_* ($R_\odot$)	M_* ($M_\odot$)	L_* ($L_\odot$)
HD 165459	11.26 ± 0.28	8420	−0.158	1.8	2.1	13 ± 1
HR 5949	6.89 ± 0.40	10010	−0.408	2.5	3.1	72^{+9}_{-8}
HD 46190	11.92 ± 0.27	8840	−0.183	2.0	2.3	15 ± 1
HR 4138	12.52 ± 0.17	9140	−0.217	2.1	2.5	79 ± 2
HD 156061	5.95 ± 0.64	4540	−0.544	17	(2)	69^{+18}_{-13}

Table 13
Dust Properties of Candidate Debris Disks

Source	Continuum range (μm)	Contrast at 30 μm (%)	T_{dust} (K)		D_{dust} (AU)		L_{dust} (10^{-4} $L_\odot$)		Min. M_{dust} (10^{-4} $M_\oplus$)
			Best	1σ range	Best	1σ range	Best	1σ range	
HD 165459	14–18	134	97	89–105	32	27–38	5.7	5.2–6.4	5.4
HR 5949	9–16	61	161	148–176	23	19–27	7.5	7.3–8.0	2.7
HD 46190	13–17	40	106	84–136	32	20–52	1.7	1.5–2.4	0.8
HR 4138	14–18	10	140	114–175	21	13–31	1.8	1.8–2.0	0.4
HD 156061	12–16	74	98	92–104	85	75–96	98	92–108	760

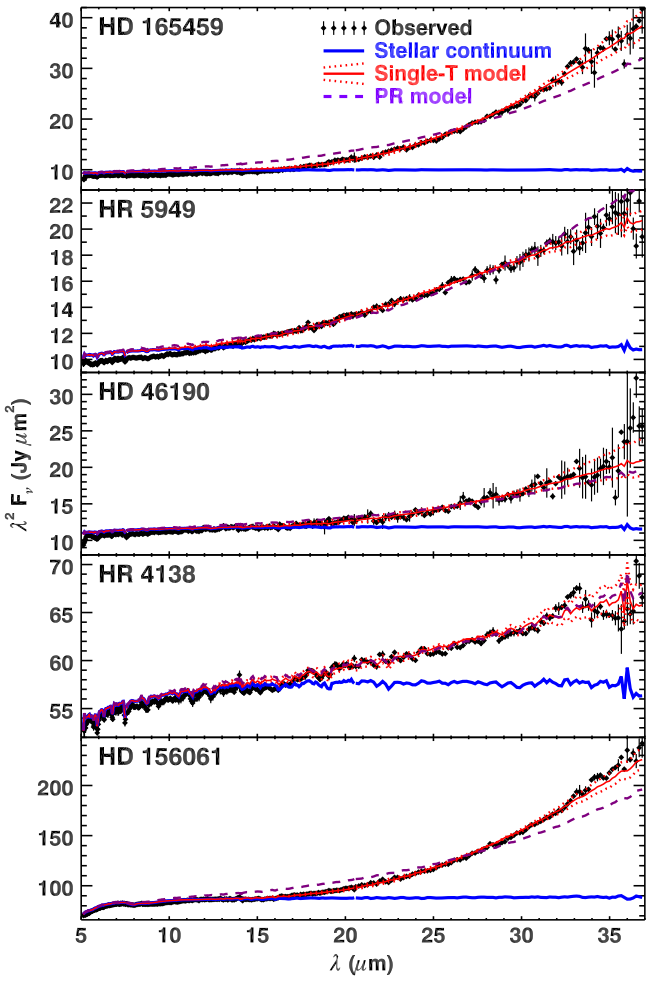

Figure 25. Possible debris disks among the IRS standards. Each panel depicts the IRS spectrum with black diamonds, the assumed continuum as a solid blue line, the single-temperature model with a solid red line, the ±1σ temperature range with dotted red lines, and the Poynting–Robertson model with a dashed purple line. This last model is only viable for HR 4138, which has the excess with the lowest contrast in the sample.

spectral templates supplied by M. Cohen. We reported these results informally (e.g., Sloan et al. 2004a, although the published abstract is non-committal). Based on the photometric analysis in Section 7, we can now conclude that the A dwarfs are at least as well behaved as the K giants. What has changed is our current focus on using the Tycho photometry to estimate expected flux densities at 22 μm. Previously, we were also considering near-infrared photometry, primarily from 2MASS (Skrutskie 2006), as well as longer-wavelength data from the *IRAS* surveys, but our sources are bright enough to saturate 2MASS, and the precision of the other infrared data does not appear to be sufficient for our purposes. We can now state that the A dwarfs are just as well behaved photometrically as the K giants, provided one has filtered out the possible debris disks.

The 24 μm dip remains an unsolved calibration problem with IRS data. While this problem does not appear to affect the four K giants with $F_{22} \lesssim 120$ mJy in our sample, the small sample size requires some caution in drawing general conclusions. Ardila et al. (2010) applied a correction to all sources in their sample fainter than 100 mJy (at 24 μm). Better understanding of this artifact awaits a more rigorous analysis of the fainter stellar spectra observed by the IRS.

9. DEBRIS DISKS

9.1. Sources with Strong Red Excesses

When selecting potential standards, we avoided sources with excesses as measured by *IRAS* at 12 and 25 μm. Nonetheless, five of the spectra in our sample show strong red excesses, which could arise from debris disks. These spectra represent 20% of our A dwarfs and 3% of our K giants. By comparison, a MIPS survey at 24 and 70 μm found debris disks around 32% of 160 stars with spectral classes between B6 and A7. Given the small size of our sample, the rate of incidence is similar. While we tried to avoid such stars, the *IRAS* 25 μm filter was too far to the blue and not sensitive enough for our purposes.

Table 12 gives the stellar properties of the five sources with possible debris disks. The parallaxes are from van Leeuwen

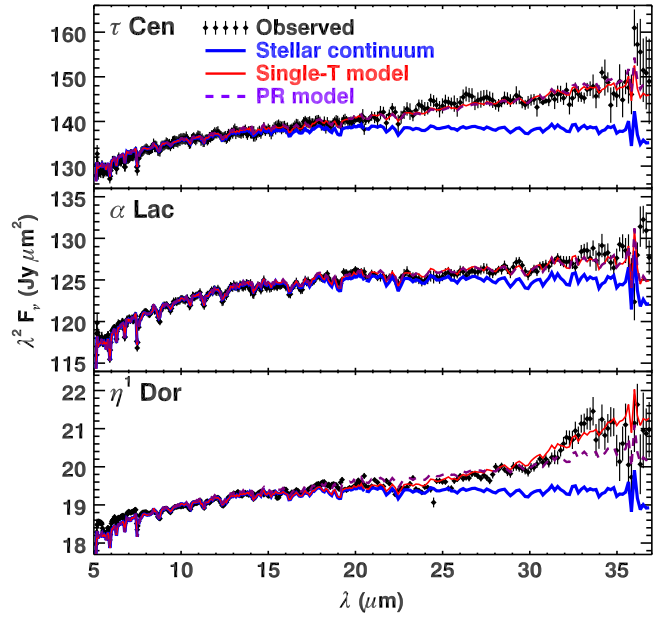

Figure 26. IRS spectra of three A dwarfs with weak excesses, showing fitted Planck functions and PR models. The spectra are noisy enough that the temperatures of the Planck functions cannot be relied on. For τ Cen, the PR model fits the excess slightly worse than the Planck function, while for α Lac, it is a slight improvement. Nothing works well for η^1 Dor, but the Planck function is the better of the two.

(2007). The effective temperatures and the bolometric corrections are interpolated using the B–V colors (Tables 9 and 10) and data from Kenyon & Hartmann (1995, Table 5). Radii and masses for the A dwarfs and all data for HD 156061 are interpolated similarly with data from Cox (2000, ApQ4). Stellar luminosities are based on the apparent V magnitudes (Tables 9 and 10), bolometric corrections, and parallaxes. The uncertainties reflect the uncertainties in parallax.

MIPS 24 μm photometry confirms the red, excesses in three of our sample stars, HD 46190, HR 4138, and HD 165459 (Engelbracht et al. 2007). Photometry at 70 μm exists only for HD 165459 (Su 2006). For temperatures above $\sim$40 K, the 70 μm point falls on the Rayleigh–Jeans side of the dust emission, and without it, our analysis is limited to the Wien side. Consequently, we have only fitted two simple models to the data: a single-temperature Planck function, simulating a population of large grains all at the same distance from the central star, and a model where Poynting–Robertson (PR) drag is feeding particles into the disk, which leads to an excess following the relation $F_\nu \propto \lambda$ (Jura 2004).

For each source, we fit the spectrum of a naked star with a similar spectral class, using δ UMi for the four A dwarfs and HR 7341 for HD 156061. We have minimized the χ^2 difference between the model and spectrum from 18 to 34 μm, allowing both the temperature of the excess and the wavelength range over which we fitted the stellar continuum to vary. We also found the temperature that produced a χ^2 value twice the minimum to estimate the 1σ spread in the likely dust temperature. Figure 25 illustrates the process, and Table 13 reports the wavelength ranges used to fit the continuum, the contrast between excess and continuum at 30 μm, and the resulting dust temperatures.

Figure 25 shows a fitted model based on PR drag using the same stellar continuum as for the single-temperature model. Only for HR 4138 is the PR-drag model as good as the single-temperature model. This star has an excess with a lower contrast than the other four debris disks, consistent with arguments by Wyatt (2005) that PR-drag should only be important in the least massive debris disks, which would be those with the lowest contrast.

If we assume that the dust grains are blackbodies in radiative equilibrium, then their distance from the central star follows the relation

$$D_{\rm dust} = \frac{R_*}{2}\left(\frac{T_{\rm dust}}{T_*}\right)^2. \quad (3)$$

Table 13 gives the distances to the dust grains ($D_{\rm dust}$) for the best-fitted dust temperature and the $\pm 1\sigma$ temperatures to either side. It also gives the corresponding dust luminosities, found by summing the single-temperature blackbodies fitted through the excesses at the wavelengths indicated. We can estimate a minimum mass using the relation given by Jura (1999),

$$M_{\rm dust} > \frac{L_{\rm dust} D_{\rm dust}^2}{G M_* c}. \quad (4)$$

Table 13 reports the lowest minimum mass from the range of likely temperatures.

Some caveats are in order. Several nearby debris disks show clear evidence for a hot inner disk (see Su 2013 and references therein) and our spectra show some evidence of a warm dust component. Our estimates of the location of the dust assume that the grains radiate as blackbodies, which is a reasonable approximation for large grains. Grains smaller than several microns will be warmer at a given distance and for a fixed temperature would have to be further away than our estimated distances.

HD 46190 illustrates the limits of our analysis for faint sources. Sloan et al. (2004) examined a version of its spectrum based on a much earlier calibration, and they found a dust temperature of 81 K, compared to the current estimate of 106 K. The temperature change has moved the dust inward, from 82 AU to 32 AU. While we are confident that a debris disk is present, our quantitative results depend strongly on the calibration and our ability to correct for the 24 μm dip.

HD 156061 is not the first red giant associated with a possible debris disk. Jura (1999) examined eight red giants with red excesses, based on their *IRAS* colors, and concluded that debris disks were better explanations of the excesses than dust outflows or the Pleaides effect (which he described as "cirrus hot spots"). Our dust-mass estimate is based on an assumed stellar mass of 2 $M_\odot$.

Sloan et al. (2004) noted that HD 46190 lies within the Local Bubble, making the Pleaides effect an unlikely explanation for the red excess in its spectrum. The same is true for HR 4138 and HD 165459. HR 5949 and HD 156061 lie beyond the boundaries of the Local Bubble. HR 5949, with a distance of 145 pc and galactic coordinates (91°, +45°), lies right in a bank of material identified in the three-dimensional maps by Lallement et al. (2003, Figure 6). HD 156061 is 180 pc away with galactic coordinates (0°, +7°), putting it in a crowded field within several degrees of the Pipe Nebula. Furthermore, red images from the Palomar Sky Survey show dust lanes within 10′ of HD 156061, but the images show no evidence for extended reflection from dust in the immediate vicinity of either HD 156061 or HR 5949. Inspection of the IRS spectral images reveals no evidence for extended emission

in LL. We conclude that the Pleaides effect is not likely for any of the five sources, although direct high-resolution imaging would be a more definitive test.

9.2. Sources with Weak Red Excesses

Several other spectra in Figures 22 and 23 show evidence of weak red excesses. The spectra of τ Cen, α Lac, and η^1 Dor have sufficient S/Ns for further analysis. Other spectra suggestive of weak excesses include 21 Lyn, ξ^1 Cen, 29 Vul, λ Tel, and HR 1014. Most of this latter group show artifacts remaining after our attempt to correct for the 24 μm dip, making further analysis inadvisable.

Figure 26 plots the spectra of τ Cen, α Lac, and η^1 Dor, along with fitted Planck functions and PR models as done for the five sources with stronger red excesses. For all three sources, the temperature of the fitted Planck function depends strongly on the wavelength range chosen for fitting the continuum, and we limit our comments to the strength of the excess.

The spectrum of τ Cen shows an excess of 4.6% at 3 μm. This spectrum is based on seven separate observations, is bright, and consistently has a red excess. The spectrum of α Lac shows a 1.3% excess at 30 μm, and it is based on 19 pointings. As already discussed, this low-contrast excess is repeatable and has forced us to modify our method of using α Lac and δ UMi to calibrate HR 6348.

The faint spectrum of η^1 Dor makes a good test case. It is based on 44 separate spectra, and the weak red excess has appeared consistently throughout the observations. Some of the spectral structure may be due to an incomplete correction for the 24 μm dip, and at the longest wavelengths, a poor S/N. Despite these problems, the red excess has a shape consisent with a debris disk, and with a 3.5% excess at 30 μm, is stronger than in α Lac.

10. SUMMARY AND CONCLUSIONS

For the spectral calibration of the IRS, we observed a large sample of potential standards. This approach proved wise, as our pre-launch plans required considerable adjustment during the cryogenic mission.

Our sample of K giants confirms what Heras et al. (2002) found with the *ISO*/SWS data: the strength of the SiO bands increases as the giants grow cooler, but with considerable scatter. This scatter persisted in the IRS sample despite our care in limiting the luminosity class to giants ("III"). Metallicity might explain the scatter, but that is an open question. The scatter in band strength limits the accuracy of the spectral templating method for K giants, which assumes that the infrared spectral properties can be predicted from the optical spectral class.

The *B*–*V* color predicts the SiO band strength better than the optical spectral class. The optical spectral classes are based on atomic lines, which arise from layers of the envelope beneath those responsible for the absorption bands.

Price et al. (2002) found that the synthetic spectra do not predict the strength of the SiO absorption band at 8 μm with sufficient accuracy to be used as truth spectra for calibration. We confirm that the synthetic spectra consistently underpredict the actual SiO band strength.

Thus the use of either synthetic spectra or spectral templates as truth spectra would introduce artifacts at the level of a few percent into the IRS database. With no reliable truth spectra for the K giants and no suitable A dwarfs available in the CVZ, we repeated the steps taken by Cohen et al. (1992a) and used A dwarfs, which are more easily modeled, to calibrate the K giants, which are more easily observed, mitigating in the process for the hydrogen recombination lines and a slight red excess in one of our A dwarfs. The resulting truth spectrum for HR 6348 has a spectroscopic fidelity better than 0.5%, except in the immediate vicinity of the Pfund-α line at 7.5 μm and where the S/N becomes an issue at the longest wavelengths. This fidelity does not include photometric uncertainties or uncertaintites in overall spectral shape.

The K giants show OH band structure in the 14–18 μm region with band depths of up to $\sim$3% of the continuum (at the resolution of LL). We failed to include these bands in earlier versions of the calibration, despite their clear presence in synthetic spectra and their confirmation with the IRS (Decin et al. 2004). This mistake led to artifacts visible in spectra with high S/Ns in earlier versions of the Cornell calibration.

The disagreement between the molecular bands in the synthetic and observed spectra increases from the SiO band at 8 μm to the OH bands at 14–18 μm. This result is consistent with arguments by van Malderen et al. (2004) that the H^- ion could be driving the effective absorbing layer higher above the photosphere with increasing wavelength, due to its increasing opacity.

The Engelke function only models the continuum of K giants, and so must be used with caution when constructing truth spectra. The long-wavelength behavior of the synthetic spectra and Engelke functions differ by only $\sim$1%, and the IRS data are unable to clearly distinguish between the two.

Our concerns about the use of synthetic spectra and spectral templates as truth spectra are limited to spectroscopic calibration, where small deviations between assumptions and reality can have a noticeable impact on data. For photometry, the resulting errors are closer to tolerances because of the lower spectral resolution, as long as one avoids filters that coincide with strong molecular bands. Thus the use of spectral templates to calibrate IRAC or synthetic spectra to calibrate photometry from the *Herschel Space Observatory* should not face the problems described in this paper.

When we decided to concentrate on A dwarfs and K giants to calibrate the IRS, we chose not to consider solar analogues because their spectra included both atomic lines and molecular bands. This logic was flawed, because the atomic lines weaken from A to G, and the absorption bands weaken from K to G. The relative weakness of both in solar analogues will make uncertainties in their strength and shape far less significant than for the classes of standards we chose. For the IRS, the real problem with solar analogues was their rarity. None with an appropriate brightness were available in the parts of the sky continuously visible from *Spitzer*.

The primary danger presented by A dwarfs is debris disks. Screening by the available photometry proved insufficient, and even then, the case of α Lac demonstrates the need for caution. While the apparent red excess is weak, it is still strong enough to affect the calibration at the longest wavelengths.

New missions bring new challenges. The sensitivity of the *James Webb Space Telescope* will force a new set of standards. Gordon & Bohlin (2011) described a plan to use a combination of white dwarfs, A dwarfs, and solar analogues, all of which are more reliably modeled than K giants. Observations of K giants

should still be included for cross-calibration with previous missions.

The *Stratospheric Observatory for Infrared Astronomy (SOFIA)* has the opposite difficulty. Its lower sensitivity has forced it to rely on much brighter standards like those listed in Table 1. The recalibration of the *ISO*/SWS spectra of several of these sources by Engelke et al. (2006) should provide truth spectra that will avoid both the limitations of synthetic spectra and the lower S/N in the original data which served as the prototypes for the spectral templates.

The observations presented were made with the *Spitzer Space Telescope*, which is operated by the Jet Propulsion Laboratory, California Institute of Technology, under NASA contract 1407. NASA provided support for this work through contract 1257184 issued by JPL/Caltech. We are deeply grateful to Lee Armus, the leader of the IRS Instrument Support Team at the SSC, for his support of the calibration effort and his determination to observe a sufficient sample of standards to ensure the quality of the IRS data. The entire astronomy community will continue to benefit from this legacy. The late Stephan Price deserves special mention for his tireless support of infrared calibration throughout his career. His spirit underlies the philosophy of this paper. Numerous members of the IRS Team have helped with the calibration of the IRS, including D. Devost, K. I. Uchida, J. Bernard-Salas, H. W. W. Spoon, and V. Lebouteiller, then at Cornell, J. Van Cleve, then at Ball Aerospace Corp., and P. W. Morris, S. Fajardo-Acosta, J. G. Ingalls, C. J. Grillmair, P. N. Appleton, and P. Ogle, then at the SSC. L. Decin and M. Cohen provided synthetic spectra and spectral templates prior to launch, which were essential to the progress we have made in calibration. P. S. Nerenberg, M. S. Keremedjiev, and D. A. Ludovici contributed to this project over the years as participants in the Research Experience for Undergraduates at Cornell funded by the NSF. In addition, we thank the anonymous referee, whose comments led to a considerably improved manuscript. This research has made use of NASA's Astrophysics Data System, the SIMBAD database, operated at Centre de Données astronomiques in Strasbourg, France, and the Palomar Sky Survey.

REFERENCES

Ardila, D. R., van Dyk, S. D., Makowiecki, W., et al. 2010, ApJS, 191, 301
Aumann, H. H., Beichman, C. A., Gillett, F. C., et al. 1984, ApJL, 278, L23
Beichman, C. A., Neugebauer, G., Habing, H. J., Clegg, P. E., & Chester, T. J. 1988, *Infrared Astronomical Satellite (IRAS)* Catalogs and Atlases Explanatory Supplement (Pasadena: JPL)
Bessell, M. 2000, PASP, 112, 773
Buscombe, W., & Morris, P. M. 1958, MNRAS, 118, 609
Buscombe, W., & Morris, P. M. 1960, MNRAS, 121, 263
Chiar, J. E., & Tielens, A. G. G. M. 2006, ApJ, 637, 774
Cohen, M., Walker, R. G., Barlow, M. J., & Deacon, J. R. 1992a, AJ, 104, 1650
Cohen, M., Walker, R. G., & Witteborn, F. C. 1992b, AJ, 104, 2030
Cohen, M., Witteborn, F. C., Carbon, D. F., et al. 1992c, AJ, 104, 2045
Cohen, M., Witteborn, F. C., Walker, R. G., Bregman, J. D., & Wooden, D. H. 1995, AJ, 110, 275
Cohen, M., Witteborn, F. C., Bregman, J. D., et al. 1996a, AJ, 112, 241
Cohen, M., Witteborn, F. C., Carbon, D. F., et al. 1996b, AJ, 112, 2274
Cohen, M., Walker, R. G., Carter, B., et al. 1999, AJ, 117, 1864
Cohen, M., Megeath, S. T., Hammersley, P. L., Martín-Luis, F., & Stauffer, J. 2003, AJ, 125, 2645
Cowley, A., Cowley, C., Jaschek, M., & Jaschek, C. 1969, AJ, 74, 375
Cox, A. N. 2000, Allen's Astrophysics Quantities (4th ed.; New York: Springer)
Decin, L., Vandenbussche, B., Waelkens, C., et al. 2003, A&A, 400, 679
Decin, L., Vandenbussche, B., Waelkens, C., et al. 2003, A&A, 400, 709
Decin, L., Morris, P. W., Appleton, P. N., Charmandaris, V., Armus, L., & Houck, J. R. 2004, ApJS, 154, 408
Decin, L., & Eriksson, K. 2007, A&A, 472, 1041
de Veaucouleurs, A. 1957, MNRAS, 117, 449
Eggen, O. J. 1950, ApJ, 111, 414
Eggen, O. 1957, AJ, 62, 45
Eggen, O. J. 1960, MNRAS, 120, 448
Eggen, O. J. 1962, RGOB, 51, 79
Eggen, O. J. 1984, ApJS, 55, 597
Engelbracht, C. W., Blaylock, M., Su, K. Y. L., et al. 2007, PASP, 119, 994
Engelke, C. W. 1992, AJ, 104, 1248
Engelke, C. W., Price, S. D., & Kraemer, K. E. 2006, AJ, 132, 1445
Evans, D. S., Laing, J. D., Menzies, A., & Stoy, R. H. 1964, RGOB, 85, 207
Gordon, K. D., & Bohlin, R. 2011, AAS, 217, 254.23
Gray, R. O. 1985, JRASC, 79, 237
Gray, R. O., Corbally, C. J., Garrison, R. F., et al. 2006, AJ, 132, 161
Halliday, I. 1955, ApJ, 122, 222
Heras, A. M., Shipman, R. F., Price, S. D., et al. 2002, A&A, 394, 539
Higdon, S. J. U., Devost, D., Higdon, J. L., et al. 2004, PASP, 116, 975
Hill, G., Gulliver, A. F., & Adelman, S. J. 2010, ApJ, 712, 250
Hog, E., Fabricius, C., & Marakov, V. V. 2000, A&A, 500, 583
Houck, J. R., Roellig, T. L., van Cleve, J., et al. 2004, ApJS, 154, 18
Houk, N. 1978, Michigan Catalogue of Two-Dimensional Spectral Types for the HD Stars, Vol. 2 (Ann Arbor, MI: Univ. of Michigan)
Houk, N., & Cowley, A. P. 1975, Univ. of Michigan Catalogue of Two-Dimensional Spectral Types for the HD Stars, Vol. 1 (Ann Arbor, MI: Univ. of Michigan)
Houk, N., & Smith-Moore, M. 1988, Michigan Catalogue of Two-dimensional Spectral Types for the HD Stars, Vol. 4 (Ann Arbor, MI: Univ. of Michigan)
Jaschek, C., & Jaschek, M. 1990, The Classification of Stars (Cambridge, UK: Cambridge Univ. Press)
Johnson, H. L., & Morgan, W. W. 1953, ApJ, 117, 313
Jura, M. 1999, ApJ, 515, 706
Jura, M., Chen, C. H., Furlan, E., et al. 2004, ApJS, 154, 453
Kenyon, S. J., & Hartmann, L. 1995, ApJS, 101, 117
Kurucz, R. L. 1979, ApJS, 40, 1
Lallement, R., Welsh, B. Y., Vergely, J. L., Crifo, F., & Sfeir, D. 2003, A&A, 411, 447
Lebouteiller, V., Bernard-Salas, J., Sloan, G. C., & Barry, D. J. 2010, PASP, 122, 231
Levato, H. 1972, PASP, 84, 584
Moore, J. H., & Paddock, G. F. 1950, ApJ, 112, 48
Morgan, W. W., Harris, D. L., & Johnson, H. L. 1953, ApJ, 118, 92
Moshir, M., Kopman, G., Conrow, T. A. O., et al. 1992, Explanatory Supplement to the *IRAS* Faint Source Survey, ver. 2, JPL D-10015 8/92 (Pasadena: JPL)
Price, S. D., Sloan, G. C., & Kraemer, K. E. 2002, ApJL, 565, L55
Rieke, G. H., Blaylock, M., Decin, L., et al. 2008, AJ, 135, 2245
Ryde, N., Lambert, D. L., Richter, M. J., & Lacy, J. H. 2002, ApJ, 580, 447
Schaeidt, S. G., Morris, P. W., Salama, A., et al. 1996, A&A, 315, L55
Shipman, R. F., Morris, P. W., Beintema, D. A., et al. 2003, The Calibration Legacy of the *ISO* Mission, ed. L. Metcalfe, A. Salama, S. B. Peschke, & M. F. Kessler, Vol. 107, (ESA SP-481; Noordwijk, The Netherlands: ESA), 3
Skrutskie, M. F., Cutri, R. M., Stiening, R., et al. 2006, AJ, 131, 1163
Slettebak, A. 1954, ApJ, 119, 146
Sloan, G. C., Charmandaris, V., Fajardo-Acosta, S. B., et al. 2004a, ApJL, 614, L77
Sloan, G. C., Nerenberg, P. S., & Russell, M. R. 2003, IRS-TR 03001: The Effect of Spectral Pointing-Induced Throughput Error on Data from the IRS (Ithaca, NY: Cornell)
Sloan, G. C., & Ludovici, D. 2011a, IRS-TR 11001: Temporal Responsivity Variations on the Red Peak-Up Sub-Array (Ithaca, NY: Cornell)
Sloan, G. C., & Ludovici, D. 2011b, IRS-TR 11002: Calibration of the Acquisition Images from the Red Peak-Up Sub-Array (Ithaca, NY: Cornell)
Sloan, G. C., & Ludovici, D. 2012a, IRS-TR 12001: Spectral Pointing-Induced Througput Error and Spectral Shape in Short-Low Order 1 (Ithaca, NY: Cornell)
Sloan, G. C., & Ludovici, D. 2012b, IRS-TR 12002: Constructing a Short-Low Truth Spectrum of the Standard Star HR 6348 (Ithaca, NY: Cornell)
Sloan, G. C., & Ludovici, D. 2012c, IRS-TR 12003: Constructing Low-Resolution Truth Spectra of the Standard Stars HR 6348 and HD 173511 (Ithaca, NY: Cornell) 173511

Sloan, G. C., Morris, P. W., Fajardo-Acosta, S. B., et al. 2004b, BAAS, 36, 722
Stephenson, C. B. 1960, AJ, 65, 60
Su, K. Y. L., Rieke, G. H., Stansberry, J. A., et al. 2006, ApJ, 653, 675
Su, K. Y. L., Rieke, G. H., Malhotra, R., et al. 2013, ApJ, 763, 118
van Leeuwen, F. 2007, Hipparcos: The New Reduction of the Raw Data, Astrophysics and Space Science Library, Vol. 350, (Berlin: Springer)
van Malderen, R., Decin, L., Kester, D., et al. 2004, A&A, 414, 677
Werner, M. W., Roellig, T. L., Low, F. J., et al. 2004, ApJS, 154, 1
Wildt, R. 1939, ApJ, 90, 611
Wyatt, M. C. 2005, MNRAS, 433, 1007
Yoss, K. M. 1961, ApJ, 134, 809